Thermo-mechanical effects of microcontinent collision on ocean-continent subduction system

Alessandro Regorda[1], Manuel Roda[1]

[1]Department of Earth Sciences, Università degli Studi di Milano, Milan, Italy

Key Points:

- The subduction dynamics is influenced by different velocities imposed on both plates in case of same overall convergent rate
- Size and location of the microcontinent and convergence velocities of both plates affect the style of the subduction zone
- The final thermal state inside the mantle wedge can be significantly affected by the presence and the dimension of the microcontinent

Corresponding author: Alessandro Regorda, `alessandro.regorda@unimi.it`

Abstract

Microcontinents are globally recognized as continental regions partially or entirely surrounded by oceanic lithosphere. Due to their positioning, they may become entangled in subduction zones and undergo either accretion or subduction. High-pressure metamorphism in subducted continental rocks support the idea that microcontinents can be subducted, regardless of their low densities. In this study, we used 2D numerical models to simulate collision of microcontinents with different sizes located at various distances from the upper plate in a subduction system characterized by different convergence velocities, in order to examine their effects on the thermo-mechanical evolution of subduction systems. Specifically, we analyzed the conditions that favor either subduction or accretion of microcontinents and investigated how their presence affects the thermal state within the mantle wedge. Our results reveal that the presence of microcontinents can lead to four styles of subduction: 1) continuous subduction; 2) continuous subduction with jump of the subduction channel; 3) interruption and restart of the subduction; 4) continental collision. We discovered that larger microcontinents and higher velocities of the subducting plate contrast a continuous subduction favoring accretion, while farther initial locations from the upper plate and higher velocities of the upper plate favor the subduction of the microcontinent. Additionally, we observed that the style of subduction has direct effects on the thermal state, with important implications for the potential metamorphic conditions recorded by subducted continental rocks. In particular, models characterized by parameters that favor the subduction of a larger amount of continental material from the microcontinent exhibit warm mantle wedges.

Plain Language Summary

Microcontinents are fragments of continents partially or entirely surrounded by an ocean. Due to the relative motion of tectonic plates, they can either be accreted to the continental plate or subducted below it. In our study, we utilized computer simulations to investigate the conditions favoring subduction or accretion and how the presence of microcontinents varying in size and location in the ocean can impact temperatures in the subduction system. Our results reveal that the presence of a microcontinent can lead to four different styles of subduction. These styles are determined by the dimension of the microcontinent, its position in the ocean, and the velocity at which it converges toward the continent: 1) uninterrupted subduction; 2) relocation of the subduction from the front to the back of the microcontinent without interruption; 3) interruption and restart of the subduction; and 4) no subduction. We observed that higher convergence velocities and a greater initial distance between the microcontinent and the continent favor uninterrupted subduction (style 1). On the other hand, larger microcontinents and higher velocities of the ocean favor the relocation or momentary interruption of the subduction (styles 2-4). Finally, we noted that microcontinents induce noticeable changes in temperatures within the subduction system.

1 Introduction

The oceanic lithosphere is characterized by lithological heterogeneities that are considered to represent remnants of extinct arcs, abandoned spreading ridges (aseismic ridges), anomalous volcanic piles, uplifted oceanic crust, and sea mounts. Sometimes even submarine regions of continental crust can occur on the oceanic plate and are subdivided into continental fragments (or ribbons) or microcontinents (Scrutton, 1976; Stein & Ben-Avraham, 2007; Vogt & Gerya, 2014). The continental fragments are bound by oceanic crust on one side and thick sedimentary basins overlying extremely thinned continental crust on the other. Microcontinents, instead, are entirely surrounded by oceanic lithosphere (Scrutton, 1976; Tetreault & Buiter, 2014). Their length varies from tens to hun-

dreds of kilometers, with a width of 20-40 km (Tetreault & Buiter, 2014; Nemčok et al., 2016).

The microcontinents, in particular, can form from passive or active margins. In the first case, during rifting, continental fragments can be separated from the continental margin and eventually become bounded by oceanic lithosphere. The formation of microcontinents at passive margins requires a combination of preexisting linear weaknesses in the continental lithosphere (van den Broek et al., 2020), rotational or oblique extension (Molnar et al., 2018), and variation in extension magnitude over time (Magni et al., 2021). The separation of microcontinents from passive margins usually occurs during the latest stages of continental breakup, before the onset of seafloor spreading (Molnar et al., 2018). However, it may also occur after the onset of seafloor spreading, due to the ridge jump onto adjacent zones of weakness when the former spreading ridge becomes amagmatic (Müller et al., 2001; Péron-Pinvidic & Manatschal, 2010; Sinha et al., 2015; Abera et al., 2016). Microcontinents can form from an active margin in a subduction setting as a result of ridge jump in back-arc basins in combination with rotational or oblique extension (van den Broek & Gaina, 2020; van den Broek et al., 2020; Magni et al., 2021) or a plume-induced break-up (Koptev et al., 2019).

Since a microcontinent is situated on an oceanic plate, it becomes entangled in subduction zones, where it can be either accreted or subducted (Tetreault & Buiter, 2012, 2014). Despite the relatively low density of continental crust, evidence supporting its subductability emerges from numerous discoveries of high-pressure mineral associations in continental rocks (Chopin, 1984; Smith, 1984; X. Wang et al., 1989; N. V. Sobolev & Shatsky, 1990; Chopin, 2003; Liu et al., 2007) and geodynamic modeling (Gerya & Stöckhert, 2006; Afonso & Zlotnik, 2011; Roda et al., 2012). This implies that lithospheric buoyancy alone is insufficient to resist subduction when considering all factors of subduction dynamics (Tetreault & Buiter, 2012). According to the analysis by Cloos (1993), the maximum thickness of subductable crustal fragments is estimated to be 15–20 km. Ellis et al. (1999) demonstrated that continental fragments measuring 30 km in thickness and 90 km in width undergo deformation and folding during subduction within the subduction channel. However, these experiments did not consider the sub-lithospheric mantle, thermal evolution, or substantial convergence rates. The nature of the subduction interface also plays a role in crust subductability (De Franco et al., 2008a, 2008b).

Previous works have analyzed the impact of various parameters on the evolution of subduction systems characterized by oceanic plateaus, seamounts, or microcontinents (e.g. De Franco et al., 2008a; Gerya et al., 2009; Tetreault & Buiter, 2012; Vogt & Gerya, 2014; Yang et al., 2018; Tao et al., 2020; Gün et al., 2022; Yan et al., 2022). However, these models typically focused on very large terranes located at significant distances () from the initial trench, emphasizing mechanical effects such as subductibility or material recycling, with less attention to thermal effects. De Franco et al. (2008b) illustrated how a subduction channel facilitates the coherent and steady-state subduction of a continental fragment, enabling subduction regardless of the geometry and strength of the incoming continental crust. In contrast, in discrete subduction faults, coherent subduction of incoming continental material occurs when the colliding terrane's continental rise is gentle. Conversely, trench locking and probable subsequent slab break-off occur if the terrane's margin is steep and the strength of its lower crust is high. Regardless of the subduction interface nature, the strength of the incoming continental crust significantly influences the accretion or subduction of the continental fragment. A weak lower crust facilitates accretion through shear delamination of the upper crust, while a strong lower crust results in a more coherent subduction of the continental fragment (De Franco et al., 2008b; Tetreault & Buiter, 2012).

While the influence of different convergence rates in ocean-continent subduction systems has been analyzed in present-day settings (Jarrard, 1986; Lallemand et al., 2005), as well as through both analogue (e.g., Schellart, 2005; Heuret et al., 2007) and numer-

ical (e.g., Roda et al., 2010; Regorda et al., 2017; Wolf & Huismans, 2019) models, a systematic analysis of the thermal and mechanical effects of convergence rate and microcontinent size on the dynamics of subduction systems in the case of microcontinent collision is still lacking. This analysis will be particularly useful when compared with the metamorphic evolution of the remnants of subducted and exhumed crustal rocks. For instance, consider the continental nappes in the axial part of the Alpine chain (e.g., Sesia-Lanzo Zone and Brianconnais nappes) that record high pressure and low temperature (HP-LT) metamorphism. These nappes are interpreted either as microcontinents that underwent subduction and subsequent exhumation (O'Brien et al., 2001; Rosenbaum & Lister, 2005; Babist et al., 2006), or as fragments of the upper plate scraped off through ablative subduction and recycled within the subduction channel (Polino et al., 1990; Spalla et al., 1996; Gerya & Stöckhert, 2006; Roda et al., 2012) during oceanic subduction. Analyzing the thermal evolution induced by microcontinent subduction can provide more insights into the interpretation of these continental nappes.

For this reason, our goals in the present work are: (i) to evaluate the effects of different velocities of both the subducting and the upper plate on subduction systems without a microcontinent, in order to create reference models to which we compare the effects of the introduction of microcontinents, and (ii) to analyze the thermo-mechanical effects induced by the collision of microcontinents of different sizes (ranging from 25 to 100 km wide) located at varying distances from the upper plate (ranging from 25 to 100 km). This analysis encompasses both the dynamics of ocean-continent subduction systems and the thermal evolution of the mantle wedge, where the burial and recycling of crustal material usually occur. In particular, we will identify in which cases the system is characterized either by a continuous subduction channel, by a detachment inside the subducted microcontinent with the development of a new deep subduction channel, by a jump of the subduction channel at surface in correspondence of the trench or by an interruption of the subduction, in order to recognize settings that allow subduction and exhumation of continental material and those characterized by accretion of the microcontinent at the trench.

In the following sections, we first provide a brief description of the numerical code and the model setup used in this study (Section 2). We then present the results obtained when changing the convergence velocities in a subduction system without a microcontinent, as well as in the case of microcontinent with different sizes (Section 3). Finally, we discuss whether each change affects the mechanical evolution of the subduction system and whether these changes influence the thermal conditions in the mantle wedge (Section 4).

2 Methods

In this work, we model the thermo-mechanical evolution of a subduction-collision system by means of the 2D finite element code FALCON (Regorda et al., 2023), which relies on the parallel version of the direct MUMPS solver (Amestoy et al., 2001, 2006). A complete description of the code and the results of all the benchmarks performed can be found in Regorda (2022). Here, we present the main features implemented in the code.

2.1 Numerical methods

FALCON solves the mass, momentum and energy conservation equations in a 2D Cartesian domain for an incompressible flow using the extended Boussinesq approxima-

tion (e.g., Christensen & Yuen, 1985; Ismail-Zadeh & Tackley, 2010), as follows:

$$\vec{\nabla} \cdot \boldsymbol{\sigma} + \rho\vec{g} = \vec{0} \tag{1}$$

$$\vec{\nabla} \cdot \vec{u} = 0 \tag{2}$$

$$\rho_0 C_p \left(\frac{\partial T}{\partial t} + \vec{u} \cdot \vec{\nabla} T \right) = \vec{\nabla} \cdot (k\vec{\nabla} T) + \rho H + 2\eta \dot{\boldsymbol{\varepsilon}}(\vec{u}) : \dot{\boldsymbol{\varepsilon}}(\vec{u}) - \alpha T \rho \vec{g} u_y \tag{3}$$

$$\boldsymbol{\sigma} = -p\mathbf{1} + 2\eta \dot{\boldsymbol{\varepsilon}}(\vec{u}) \tag{4}$$

$$\dot{\boldsymbol{\varepsilon}}(\vec{u}) = \frac{1}{2} \left(\vec{\nabla}\vec{u} + (\vec{\nabla}\vec{u})^T \right) \tag{5}$$

$$\rho(T) = \rho_0(1 - \alpha(T - T_0)) \tag{6}$$

where $\boldsymbol{\sigma}$ is the stress tensor, ρ is the density, $\vec{g}$ is the gravitational acceleration vector, $\vec{u}$ is the velocity, ρ_0 is the reference density, C_p is the isobaric heat capacity, T is the temperature, t is time, k is the thermal conductivity, H is the volumetric heat production, η is the (effective) viscosity, $\dot{\boldsymbol{\varepsilon}}$ is the strain rate tensor, α is the thermal expansion coefficient, and p is the pressure.

We used $Q_1 \times P_0$ elements (quadrilateral bilinear velocity-constant pressure; e.g., Thieulot & Bangerth, 2022) and, since they do not satisfy the Ladyzhenskaya, Babuska and Brezzi (LBB) stability condition (Donea & Huerta, 2003) and they are prone to element-wise checkerboard pressure pattern (van Zelst et al., 2022), the elemental pressure is smoothed by interpolating it onto nodes and then back onto elements and markers (Thieulot, 2014). The code implements the so-called penalty formulation for which the flow is very weakly compressible, so that Equation 2 can be replaced by

$$\vec{\nabla} \cdot \vec{u} = -\frac{p}{\lambda} \tag{7}$$

where λ is the penalty coefficient that has the same units as viscosity and it is required to be between 5 and 8 orders of magnitude larger than the dynamic viscosity η. A dimensionless coefficient λ^* (here fixed to 10^6) is then used so that the penalty factor is calculated for each element as $\lambda(e) = \lambda^* \eta(e)$ (Donea & Huerta, 2003; Marotta et al., 2006; Bollino et al., 2022). This method allows us to eliminate the pressure from the momentum equation 1 resulting in:

$$\lambda\vec{\nabla}(\vec{\nabla} \cdot \vec{u}) + \vec{\nabla} \cdot \eta \left(\vec{\nabla}\vec{u} + (\vec{\nabla}\vec{u})^T \right) + \rho\vec{g} = \vec{0} \tag{8}$$

This equation is then solved for the velocity field, while the pressure can be recovered as a post-processing step using Equation 7.

The time step is calculated by means of the Courant-Friedrichs-Lewy (CFL) condition (Anderson, 1995):

$$\delta t = C \min\left(\frac{h_m}{u_M}, \frac{h_m^2}{\kappa} \right) \tag{9}$$

with C is the dimensionless Courant number between 0 and 1, $h_m = \min_\Omega(h)$ is the dimension of the smallest element in the mesh, $u_M = \max_\Omega |\vec{u}|$ is the maximum velocity in the domain, κ is the heat diffusion (typically around 1×10^{-6} m^2 s^{-1} in lithospheric-scale models). The (nonlinear) mass and momentum conservation equations are then solved at each time step δt, followed by the energy equation. The streamline-upwind Petrov–Galerkin (SUPG) method is implemented in the energy equation to stabilize advection (Hughes & Brooks, 1982; Thieulot, 2011). Materials are subsequently advected and topography updated. Surface processes at the free surface have been implemented by means of the software Fastscape (Braun & Willett, 2013; Cordonnier et al., 2019; Yuan, Braun, Guerit, Rouby, & Cordonnier, 2019; Yuan, Braun, Guerit, Simon, et al., 2019).

Materials are tracked by means of the Particle-in-Cell method. A regularly distributed swarm of Lagrangian markers covers the entire domain and their advection is performed by means of a 2nd-order Runge-Kutta scheme in space. The interpolated velocity is then

180 corrected by means of the Conservative Velocity Interpolation (CVI; H. Wang et al., 2015).
181 Each marker tracks a given material type and the total number of markers in each el-
182 ement is maintained between a minimum ($n_{\min}$) and a maximum ($n_{\max}$) value. Elemen-
183 tal properties, except for the viscosity, are calculated as the arithmetic average on all the
184 markers inside each element.

185 FALCON implements the Arbitrary Lagrangian Eulerian (ALE; Donea et al., 2004)
186 formulation to accommodate topography by means of free surface deformation: the sides
187 and bottom boundaries remain straight and the length of the domain in the x-direction
188 does not change (kinematic boundary conditions on these boundaries thereby imply a
189 flux of material through the boundary). However, the top boundary deforms using the
190 velocity field as it is resampled at equidistant abscissae with vertical adjustment of grid
191 nodes in each column at equidistant ordinates and topography is thus created (Thieulot,
192 2011). To avoid the drunken-sailor instability, the free surface stabilization algorithm of
193 Kaus et al. (2010) is implemented.

194 The viscosities for dislocation (ds) and diffusion (df) creep are given by

$$\eta_{\mathrm{ds}} = \left(\frac{1}{A_{\mathrm{ds}}}\right)^{\frac{1}{n_{\mathrm{ds}}}} \dot{\varepsilon}_e^{\frac{1-n_{\mathrm{ds}}}{n_{\mathrm{ds}}}} \exp\left(\frac{Q_{\mathrm{ds}} + pV_{\mathrm{ds}}}{n_{\mathrm{ds}}RT}\right) \tag{10}$$

$$\eta_{\mathrm{df}} = \frac{d^m}{A_{\mathrm{df}}} \exp\left(\frac{Q_{\mathrm{df}} + pV_{\mathrm{df}}}{RT}\right) \tag{11}$$

(e.g., Gerya & Stöckhert, 2002; Billen & Hirth, 2007; Arredondo & Billen, 2016),
where A, n, Q, V are material dependent parameters. A is the pre-exponential factor, n
is the stress exponent, Q is the activation energy, V is the activation volume, R is the
gas constant, d is the grain size, m is the grain size exponent and $\dot{\varepsilon}_e = \sqrt{I_2(\dot{\boldsymbol{\varepsilon}})}$ is the
effective strain rate, given as the square root of the second invariant of the strain rate
tensor. Note that diffusion creep is considered in the sublithospheric mantle only and
in this case the stress exponent is $n = 1$, so that the corresponding viscosity does not
depend on the strain rate. Since both types of viscous creep act simultaneously within
the lithosphere under the same deviatoric stress (Karato, 2008; Glerum et al., 2018), the
composite viscous creep η_{cp} is then calculated as the harmonic average between η_{df} and
η_{ds} (e.g., Duretz et al., 2011; Arredondo & Billen, 2016; Glerum et al., 2018):

$$\eta_{\mathrm{cp}} = \left(\frac{1}{\eta_{\mathrm{df}}} + \frac{1}{\eta_{\mathrm{ds}}}\right)^{-1} \tag{12}$$

To approximate brittle behavior in our models, a Drucker-Prager plasticity crite-
rion is used (e.g., Alejano & Bobet, 2012; Quinquis & Buiter, 2014; Le Pourhiet et al.,
2017; Glerum et al., 2018), given by

$$\eta_{\mathrm{p}} = \frac{p\sin\phi + c\cos\phi}{2\dot{\varepsilon}_e} \tag{13}$$

where c is the cohesion and ϕ the angle of friction. The effective viscosity value is then
computed assuming that creep mechanisms and plasticity are independent processes (e.g.,
Karato, 2008; Andrews & Billen, 2009; Glerum et al., 2018), that is

$$\eta_{\mathrm{eff}} = \min\left(\eta_{\mathrm{cp}}, \eta_{\mathrm{p}}\right) \tag{14}$$

195 In order to keep this viscosity within meaningful bounds it is limited to remain in the
196 range $[\eta_{\min}, \eta_{\max}]$, with typically $\eta_{\min} = 1 \times 10^{19}\,\mathrm{Pa\,s}$ and $\eta_{\max} = 1 \times 10^{25}\,\mathrm{Pa\,s}$. The ef-
197 fective viscosity η_{eff} is calculated interpolating effective strain rates, pressures and tem-
198 peratures of the nodes onto the markers. Elemental viscosities are then calculated as the
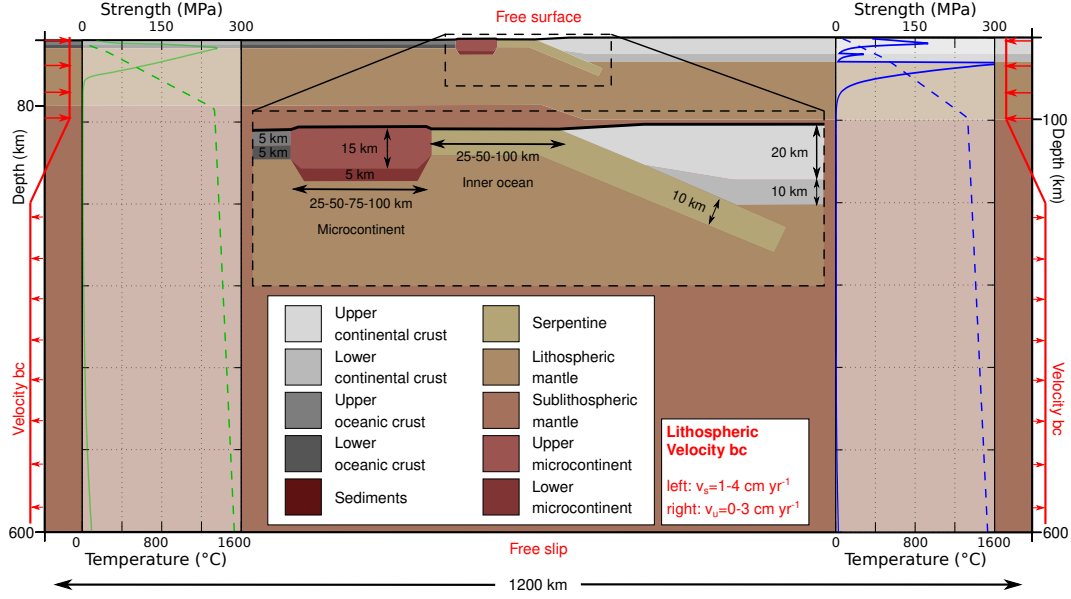199 geometric average of η_{eff} of the markers inside each element.

Figure 1. Model setup showing crust and mantle lithosphere layer thicknesses with the corresponding temperature (dashed) and strength (continuous) profiles (blue and green for the continental and oceanic domain, respectively). The velocity boundary conditions are in red.

Strain softening is taken into account for both plasticity and viscous creep (Huismans & Beaumont, 2003; Babeyko & Sobolev, 2005; Huismans et al., 2005; S. V. Sobolev & Babeyko, 2005; Warren et al., 2008) by means of the accumulated strain ε_p and ε_v, respectively, memorized by each marker. Plastic weakening approximates deformation-induced softening of faults and brittle shear zones, while viscous weakening can be interpreted as strain-induced grain size reduction and effects of synkinematic metamorphic reactions (Warren et al., 2008). Plastic weakening is simulated by a linear decrease with the strain of cohesion and angle of friction values, when $\varepsilon_{p1} < \varepsilon_p < \varepsilon_{p2}$. Similarly, viscous weakening linearly reduces the viscosity when the viscous strain ε_v is between ε_{v1} and ε_{v2} (Huismans & Beaumont, 2003; Warren et al., 2008).

2.2 Numerical setup

In this study, we use different setups with various dimensions both of the microcontinent and of the inner oceanic domain (Figure 1), in an experimental domain of 1200×600 km. The minimum numerical resolution is 5×5 km with a horizontal refinement towards the center of the model (between $x = 400$ and $x = 800$ km) and a vertical refinement towards the surface (above 120 km depth) where the maximum resolution is 1×1 km. The total number of elements is 163,200 and each element is initialized with 16 markers that allow for the tracking of different materials throughout the experiments. For time-stepping we use a Courant number of 0.25.

The initial thermal structure of the lithosphere corresponds to a simple conductive thermal configuration, with a fixed surface temperature of 0 °C and a temperature of 1330 °C at its base (e.g., Erdős et al., 2019; Marotta et al., 2020; Regorda et al., 2021, 2023). The temperature of the sublithospheric mantle follows an adiabatic gradient of $0.4 °C \, km^{-1}$ that leads to a temperature of 1530 °C at 600 km depth (e.g., Salazar-Mora et al., 2018; Theunissen & Huismans, 2019). No heat flow is allowed across the side boundaries. All the rheological and thermal parameters can be found in Table 1.

Table 1. Densities and plastic, viscous, and thermal parameters of the materials used in the models. Crustal and lithospheric thicknesses in brackets refer to the microcontinents. The variation of the sublithospheric thicknesses refer to domains below continental and oceanic lithospheric mantle, respectively.

Parameter	Symbol	Units	Continental Crust Upper	Continental Crust Lower	Oceanic Crust Upper	Oceanic Crust Lower	Sediments	Serpentine	Mantle Lithospheric	Mantle Sublithospheric
Thickness	-	km	20 (15)	10 (5)	5	5	-	-	70 (60)	500-520
Density[a,b,c,d]	ρ	$\mathrm{kg\,m^{-3}}$	2750	2900	3200		2650	3000	3300	
Plastic weakening range[e]	ε_{p1}-ε_{p2}	-	0.5-1.5		0.5-1.5		0.5-1.5	0.5-1.5	0.5-1.5	
Friction angle[f]	ϕ	°	25-5		15-3	25-5	25-5	25-5	25-5	
Cohesion[e,f]	c	MPa	20-4		10-2	20-4	20-4	20-4	20-4	
Viscous weakening range[f]	ε_{v1}-ε_{v2}	-	1-5		1-5		1-5	1-5	1-5	
Viscous weakening factor[f]	f_{vw}	-	10		10		10	10	10	
Flow law*			Dry granite[g]	Felsic granulite[h]	Antigorite[a]	Microgabbro[h,i]	Wet granite[g]	Antigorite[a]	Dry olivine[l]	
Dislocation creep										
Pre-exponential factor	A_{ds}	$(\mathrm{Pa\,s^{-1}})$	1.14×10^{-28}	2×10^{-21}	1.39×10^{-37}	1.99×10^{-11}	7.96×10^{-16}	1.39×10^{-37}	1.1×10^{-16}	
Stress exponent	n_{ds}	-	3.2	3.1	3.8	3.4	1.9	3.8	3.5	
Activation energy	Q_{ds}	$(\mathrm{kJ\,mol^{-1}})$	123	243	89	497	140	89	530	
Activation volume	V_{ds}	$(\mathrm{m^3\,mol^{-1}})$	0		0.32×10^{-5}	0	0	0.32×10^{-5}	1.8×10^{-5}	
Diffusion creep										
Pre-exponential factor	A_{df}	$(\mathrm{Pa\,s^{-1}})$	-		-		-	-	-	2.37×10^{-15}
Activation energy	Q_{df}	$(\mathrm{kJ\,mol^{-1}})$	-		-		-	-	-	375
Activation volume	V_{df}	$(\mathrm{m^3\,mol^{-1}})$	-		-		-	-	-	1×10^{-5}
Grain size	d	(mm)	-		-		-	-	-	5
Grain size exponent	m	-	-		-		-	-	-	3
Thermal parameters										
Heat capacity[a,f,m]	C_p	$(\mathrm{m^2\,K\,s^{-2}})$	800		800		800	1250	1250	
Conductivity[a,d]	k	$(\mathrm{W\,m^{-1}\,K^{-1}})$	3.2	2.1	1.8	2.6	3.2	2.25	2.25	
Thermal expansion[a,f]	α	$(\mathrm{K^{-1}})$	3.28×10^{-5}		3.28×10^{-5}		3.28×10^{-5}	3×10^{-5}	3×10^{-5}	
Heat production[d,e]	H	$(\mathrm{\mu W\,m^{-2}})$	1.3		0.2		1.3	0	0	

* The Stokes solver tolerance and the maximum number of iterations have been fixed to 10^{-3} and 100, respectively.

References: [a]Petersen and Schiffer (2016); [b]Gerya et al. (2004); [c]Gerya and Yuen (2003); [d]Naliboff and Buiter; [e]Naliboff et al. (2020); [f]Warren et al. (2008); [g]Ranalli (1995); [h]Wilks and Carter (1990); [i]Burov (2011); [l]Hirth and Kohlstedt (2003); [m]Rolf et al. (2018).

We consider a 20 km thick upper continental crust with a 10 km thick lower continental crust for the upper plate, and a 5 km thick upper oceanic and a 5 km thick lower oceanic crust for the subducting plate. We also consider a 70 km thick lithospheric mantle for both plates, resulting in a 100 km thick lithosphere for the upper plate and in a 80 km thick lithosphere for the subducting plate. The microcontinents are placed on the subducting plate and they are characterized by a 15 km thick upper crust and a 5 km thick lower crust on top of a 60 km thick lithospheric mantle (Table 1 and Figure 1). In order to initiate the subduction, we use a weak seed between the upper and lower plate, consisting of a 10 km thick serpentine layer up to 50 km depth, that will eventually evolve into a subduction channel (e.g., De Franco et al., 2008a; Tetreault & Buiter, 2012). The initial topography is given by the isostatic re-equilibration of the system.

Here, we tested microcontinents of various dimensions (25, 50, 75, and 100 km) placed at different distances from the continental plate (inner ocean size: 25, 50, and 100 km). We also examined different inflow velocities set along both vertical boundaries. We set inflow velocities from the surface down to the bottom of the lithosphere at 1 and 4 $\mathrm{cm\,yr^{-1}}$ on the left side of the domain (subducting oceanic plate) and 0 and 3 $\mathrm{cm\,yr^{-1}}$ on the right side (upper continental plate). The velocities on the oceanic plate were chosen to simulate slow and intermediate subductions. A velocity of 3 $\mathrm{cm\,yr^{-1}}$ on the continental plate was selected to analyze the effects of the upper plate movement, considering velocities higher or lower than the subducting plate. Moreover, these velocities allow us to investigate whether the geodynamics of the subductive system is affected solely by the total convergent velocity or the distribution of velocities among the plates also influences the thermo-mechanics of the system. In all models, a constant outflow velocity along the vertical boundaries in the asthenosphere and a linear transitional zone of 100 km were set, ensuring that the net material flux along the vertical boundaries is 0. The models evolved for different times required to achieve a final convergence of 300 km. All the simulations tested are summarized in Table 2.

3 Results

Throughout this work, the models are identified by their unique model identifier, as shown in the first column of Table 2 that provides information about the dimension of the microcontinent (MC), followed by indicators of the dimension of the inner ocean (IO) between the microcontinent and the upper plate, and the velocities of both the subducting (vs) and the upper (vu) plates. For example, the identifier $S9_{25}.IO_{100}.vs_1.vu_0$ is used for a model with a small (S9) microcontinent (25 km), an inner ocean of 100 km (IO_{100}), a subducting plate velocity (vs) of 1 $\mathrm{cm\,yr^{-1}}$, and an upper plate velocity (vu) of 0 $\mathrm{cm\,yr^{-1}}$. In case of models without microcontinent (models NM), the model identifier is only followed by the the plates velocities.

Firstly, we present the results of models without a microcontinent (models NM in Table 2) to verify whether different velocities of both plates affect the thermo-mechanical evolution of the subduction system. Subsequently, we present the modeling results for: 1) models with small microcontinents (25 km; models S in Table 2); 2) models with medium microcontinents (50 km; models M in Table 2); 3) models with large microcontinents (75 km; models L in Table 2); and 4) models with extra-large microcontinents (100 km; models XL in Table 2).

For all these models, we first discuss the cases with a narrow inner ocean (25 km-wide), comparing their thermo-mechanical evolution with models without microcontinents characterized by the same velocities (models NM in Table 2). After that, we analyze the thermo-mechanical impact of different dimensions of the inner ocean (50 and 100 km). The effects on the thermal state are analyzed through three geotherms located at 50, 75, and 100 km from the trench, identified as geotherm$_{50}$, geotherm$_{75}$, and geotherm$_{100}$, respectively. All geotherms have been calculated exclusively above the slab to highlight

Table 2. Setup for the different models tested. The following parameters have been varied: dimension of the microcontinent (MC); dimension of the inner ocean (IO) located between the microcontinent and the upper plate; upper plate (UP) velocity; subducting plate (SP) velocity; duration of the evolution (model time). The models are shown in the figures listed in the last column.

Model	MC dimension (km)	IO dimension (km)	SP velocity (cm yr^{-1})	UP velocity (cm yr^{-1})	Model time (Myr)	Figures
NM1	1	0	-	-	30	Figure 2a, e and i
NM2	1	3	-	-	7.5	Figure 2b, f and l
NM3	4	0	-	-	7.5	Figure 2c, g and m
NM4	4	3	-	-	4.5	Figure 2d, h and n
S1	25	25	1	0	30	Figure 3a and e
S2	25	25	1	3	7.5	Figure 3b and f
S3	25	25	4	0	7.5	Figure 3c and g
S4	25	25	4	3	4.5	Figure 3d and h
S5	25	50	1	0	30	Figure 5a and d
S6	25	50	1	3	7.5	-
S7	25	50	4	0	7.5	-
S8	25	50	4	3	4.5	-
S9	25	100	1	0	30	Figure 5b and e
S10	25	100	1	3	7.5	-
S11	25	100	4	0	7.5	Figure 5c and f
S12	25	100	4	3	4.5	-
M1	50	25	1	0	30	Figure 6a, e and i
M2	50	25	1	3	7.5	Figure 6b, f and l
M3	50	25	4	0	7.5	Figure 6c, g and m
M4	50	25	4	3	4.5	Figure 6d, h and n
M5	50	50	1	0	30	-
M6	50	50	1	3	7.5	Figure 8a, e and i
M7	50	50	4	0	7.5	-
M8	50	50	4	3	4.5	-
M9	50	100	1	0	30	Figure 8b, f and l
M10	50	100	1	3	7.5	Figure 8c, g and m
M11	50	100	4	0	7.5	Figure 8d, h and n
M12	50	100	4	3	4.5	-
L1	75	25	1	0	30	-
L2	75	25	1	3	7.5	-
L3	75	25	4	0	7.5	Figure 9a, c and e
L4	75	25	4	3	4.5	Figure 9b, d and f
L5	75	50	1	0	30	-
L6	75	50	1	3	7.5	-
L7	75	50	4	0	7.5	Figure 11a, d and g
L8	75	50	4	3	4.5	-
L9	75	100	1	0	30	-
L10	75	100	1	3	7.5	-
L11	75	100	4	0	7.5	Figure 11b, e and h
L12	75	100	4	3	4.5	Figure 11c, f and i
XL1	100	25	1	0	30	Figure 12a, e and i
XL2	100	25	1	3	7.5	-
XL3	100	25	4	0	7.5	-
XL4	100	25	4	3	4.5	-
XL5	100	50	1	0	30	-
XL6	100	50	1	3	7.5	-
XL7	100	50	4	0	7.5	Figure 12b, f and l
XL8	100	50	4	3	4.5	-
XL9	100	100	1	0	30	-
XL10	100	100	1	3	7.5	-
XL11	100	100	4	0	7.5	Figure 12c, g and m
XL12	100	100	4	3	4.5	Figure 12d, h and n

differences in the thermal state of the mantle wedge, which are crucial for understanding the metamorphic evolution of subducted and exhumed crustal rocks. These geotherms are presented from the surface to 25, 45, and 80 km depth for geotherm$_{50}$, geotherm$_{75}$, and geotherm$_{100}$, respectively.

3.1 Models without microcontinent - models NM

3.1.1 Model with v_s=1 $\mathrm{cm\,yr}^{-1}$ and v_u=0 $\mathrm{cm\,yr}^{-1}$ - model NM1

The reference model NM1, characterized by a slow subducting plate velocity (v_s=1 $\mathrm{cm\,yr}^{-1}$) and a fixed upper plate velocity (v_u=0 $\mathrm{cm\,yr}^{-1}$), exhibits the classical evolution of subduction systems. It shows the development of a subduction channel characterized by high strain rates (exceeding $10^{-14}\,\mathrm{s}^{-1}$), which facilitates the initiation of subduction (blue-to-white area in Fig. 2a and Movie S1 in the Supporting Information).

During the initial phase, the coupling between the two plates results in elevated topography in the forearc region and a slight advancement of the trench (approximately 30 km; indicated by the red star in Fig. 2i). This phase concludes when a continuous subduction channel forms up to the bottom of the lithosphere. However, the coupling is not strong enough to induce ablation of continental crust from the upper plate, resulting in no recycling of continental crust in the wedge.

Subsequently, the trench experiences slow retreat (approximately 30 km) due to the collapse of the topography developed in the forearc, leading to the advancement of the accretionary wedge toward the subducting plate (indicated by the green star in Fig. 2i). During the second half of the evolution, as the subduction channel becomes well-formed and continuous (Fig. 2e and Movie S1 in the Supplementary Information), all forces balance out, and both the trench and the topography show no further variation (Fig. 2i).

3.1.2 Effects of plates velocities - models NM2-NM4

The imposition of a velocity on the upper plate (model $NM2.vs_1.vu_3$) results in higher coupling between the plates, leading to the development of a higher strain rate in the forearc region during the initial phase of the evolution (Fig. 2b). However, due to the higher value of v_u compared to v_s (v_s=1 $\mathrm{cm\,yr}^{-1}$ and v_u=3 $\mathrm{cm\,yr}^{-1}$), this model does not exhibit any advancement of the trench, which consistently retreats for the entire duration of the simulation (approximately 200 km; Fig. 2l), in contrast to the behavior observed in model NM1. On the contrary, the evolution of the topography is characterized by a continuous decrease in the maximum height after the development of a continuous subduction channel (Fig. 2l), as observed in model NM1. The continuous advancement of the upper plate results in a decrease in the dip angle of the shallowest portion of the slab (above 50 km), which is 24° (Fig. 2f), compared to 28° calculated in the model with the fixed upper plate (model NM1; Fig. 2e). Nevertheless, the final dynamics are similar to that observed in model NM1, with no ablation of continental crust from the upper plate.

Model $NM3.vs_4.vu_0$ is characterized, like model NM2, by a total convergent velocity of 4 $\mathrm{cm\,yr}^{-1}$ (v_s=4 $\mathrm{cm\,yr}^{-1}$ and v_u=0 $\mathrm{cm\,yr}^{-1}$). However, the coupling between the plates and the general dynamics are remarkable different from the previous model. Model NM3 shows the development of bands with high strain rates that cross the entire thickness of the continental crust of the upper plate during the initial phase of the evolution (Fig. 2c and Movie S2 in the Supplementary Information), as a result of higher coupling compared to models NM1 and NM2 (Fig. 2a and b, respectively). Consequently, the maximum topography developed is higher, and there is an initial advancement of the trench of approximately 100 km, marked by a red star in Fig. 2m. The higher coupling also results in the ablation of upper and lower continental crust from the upper plate,
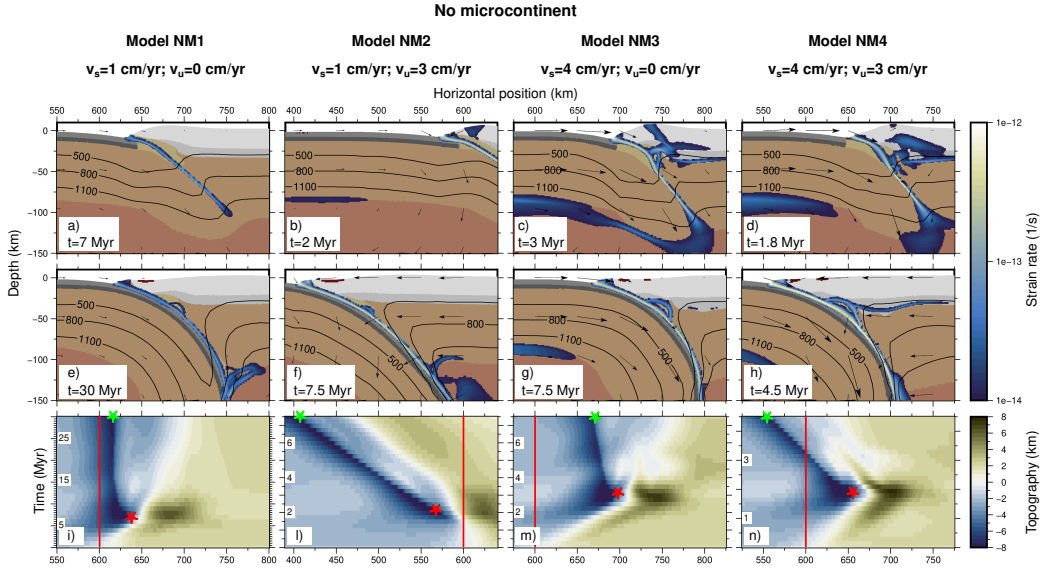
Figure 2. The evolution of models without a microcontinent at two distinct stages, including velocity fields and strain rates (panels a-h), and the evolution of topography throughout the entire duration of simulations (panels i-n) are presented for different velocities of the subducting plate (v_s) and the upper plate (v_u). Black lines on the figures indicate 500, 800, and 1100 °C isotherms, while background colors define the composition as in Fig. 1. Red lines indicate the initial position of the trench, and red stars represent the trench position at the time shown in the first row, indicating the maximum advancement. Green stars indicate the maximum retreat of the trench.

leading to slight recycling in the wedge during the second half of the evolution (Fig. 2g), unlike models NM1 and NM2. However, the second part of the simulation is similar to what was observed for the previous models, with a continuous collapse of the topography of the upper plate that leads to a slight retreat of the trench (approximately 30 km; Fig. 2m). The final geometry of the slab is also similar to that of the reference model (NM1), with a shallow dip angle of the slab of 28° (Fig. 2g)

Model $NM4.vs_4.vu_3$ (v_s=4 cm yr^{-1} and v_u=3 cm yr^{-1}) exhibits characteristics found both in model NM2 and in models NM1 and NM3. In fact, high velocities imposed on both plates result in high strain rates in the upper plate (Fig. 2d) and, consequently, high topography (Fig. 2n), similar to the pattern observed in model NM3 (Fig. 2m). Similarly, the higher velocity of the subducting plate leads to an initial advancement of the trench (approximately 60 km) in the initial 2 Myr of evolution (red star in Fig. 2n), resembling the behavior of models NM1 and NM3 (red stars in Fig. 2i and m). However, the imposed velocity on the upper plate limits this advancement, which is less than in model NM3, and results in a pronounced trench retreat in the second half of the simulation (approximately 100 km; green star in Fig. 2n), akin to the behavior observed in model NM2 characterized by low v_s and high v_u (Fig. 2l). This is related, as in the previous models, to the development of a continuous subduction channel (Fig. 2h) that leads to a decrease in strain rates in the upper plate and the consequent collapse of the topography (Fig. 2n). Lastly, the velocity imposed on the upper plate causes a decrease in the shallow slab dip, albeit to a limited extent due to the high velocity of the subducting plate. The final dip angle is 26°, between the angles calculated for models NM1 and NM3 (28°) and for model NM2 (24°).

3.2 Models with 25 km-wide microcontinent - models S

3.2.1 Models with 25 km-wide inner ocean - models S1-S4

In cases involving models with small microcontinents (25 km-wide) and a narrow inner ocean (25 km-wide; models S1-S4 in Fig. 3), the microcontinents do not accrete at the trench. Consequently, the accretionary wedge is primarily composed of sediments, resembling the models without microcontinents (refer to models NM1-NM4 in Fig. 2). As a result, a significant amount of continental material is subducted and subsequently exhumed in the mantle wedge (Fig. 3a-d). Differences emerge in the ability to recycle and eventually exhume subducted material, influenced by variations in the velocities of the subducting and upper plates.

In particular, for $v_s = 1$ cm yr^{-1} and a fixed upper plate (model $S1_{25}.IO_{25}.vs_1.vu_0$), there is exhumation of almost the entire microcontinent, rising from a maximum depth of approximately 140 km to 10-15 km depth (Fig. 3a and Movie S3 in the Supporting Information). This exhumation occurs due to a detachment between upper and lower crust of the microcontinent when it is already subducted (at approximately 40 km depth), facilitating detachment from the slab and subsequent recycling. The exhumation of a significant amount of continental material promotes the upwelling of subducted oceanic material and has a slight effect on the shallow slab dip angle, decreasing from 28° in model NM1 to 25°. During the first half of evolution, the subduction of the microcontinent does not affect neither the trench advancement nor the topography with respect to model NM1 (Fig. 3e). However, model S1 exhibits an additional retreat of the trench during the last 7 million years of evolution (yellow star in Fig. 3e), attributed to the upwelling of material pushing the accretionary wedge toward the subducting plate (Fig. 3a and Movie S3 in the Supporting Information). As a consequence, the topography in the upper plate undergoes changes, marked by the formation of a pronounced basin on the forearc.

The upwelling flow to shallow depths, resulting from the exhumation of continental material in the internal portion of the mantle wedge (profiles p_1 and p_2 in Fig. 3a), together with higher radiogenic heating, induces a temperature increase of approximately
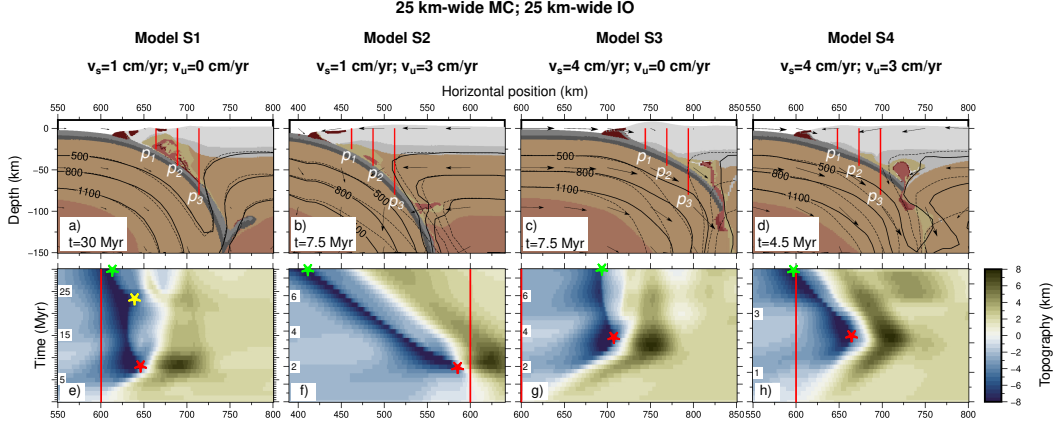
Figure 3. The evolution of models with a 25 km-wide microcontinent (MC) and a 25 km-wide inner ocean (IO), including velocity fields and strain rates (panels a-d), and the evolution of topography throughout the entire duration of simulations (panels e-h) are presented for different velocities of the subducting plate (v_s) and the upper plate (v_u). Red lines on panels a-d (p_1, p_2 and p_3) indicate the position of the thermal profiles shown in Fig. 4. Black lines indicate 500, 800 and 1100 °C isotherms, while dashed black lines indicate the same isotherms referred to NM1 model. Background colors define the composition as in Fig. 1. In panels e-h, red lines and red stars indicate the initial position and the maximum advancement of the trench, respectively, while the green stars indicate the maximum retreat of the trench. Yellow star indicates the beginning of exhumation of subducted material.

50 °C in the mantle wedge up to 75 km from the trench (continuous light blue lines in Fig. 4a and b), compared to the model without the microcontinent (model NM1; continuous black lines in Fig. 4a and b). In contrast, the dynamics in the mantle wedge at 100 km from the trench is not affected by the exhumation of continental material (profile p_3 in Fig. 3a), resulting in no difference in the thermal state compared to model NM1 (see continuous light blue and black lines in Fig. 4c).

Conversely, a velocity on the upper plate higher than that on the subducting plate (model $S2_{25}.IO_{25}.vs_1.vu_3$; $v_s = 1$ and $v_u = 3$ cm yr^{-1}) induces a more vigorous mantle flux in the mantle wedge compared to the preceding model (model S1), which limits the recycling of subducted material (Fig. 3b). As the exhumation of material is limited, it has no effects on the topography (Fig. 3f) compared to the topography evolution observed for model NM2 (Fig. 2l). Similarly, the slab dip angle above 50 km depth remains the same as in the model without the microcontinent (24°). However, there is a clear increase in the dip angle below 50 km depth, which is easily recognizable when comparing the isotherms in Fig. 3b.

The thermal state in the internal portion of the mantle wedge (profiles p_1 and p_2 in Fig. 3b) is only slightly higher than in model NM2 (less than 50 °C). This modest increase is due to the limited amount of recycled material, evident in the geotherm50 and geotherm75 at depths below 35-40 km. As observed in model S1, the thermal state in the external portion of the wedge (profile p_3 in Fig. 3b) is the same as in model NM2.

The evolution of models with $v_s = 4$ cm yr^{-1} (models $S3_{25}.IO_{25}.vs_4.vu_0$ and $S4_{25}.IO_{25}.vs_4.vu_3$) is very similar and is not influenced by the velocity of the upper plate. Both models exhibit the exhumation of continental crust, originating from both the microcontinent and ablated from the upper plate (Fig. 3c and d). This is attributed to the higher coupling
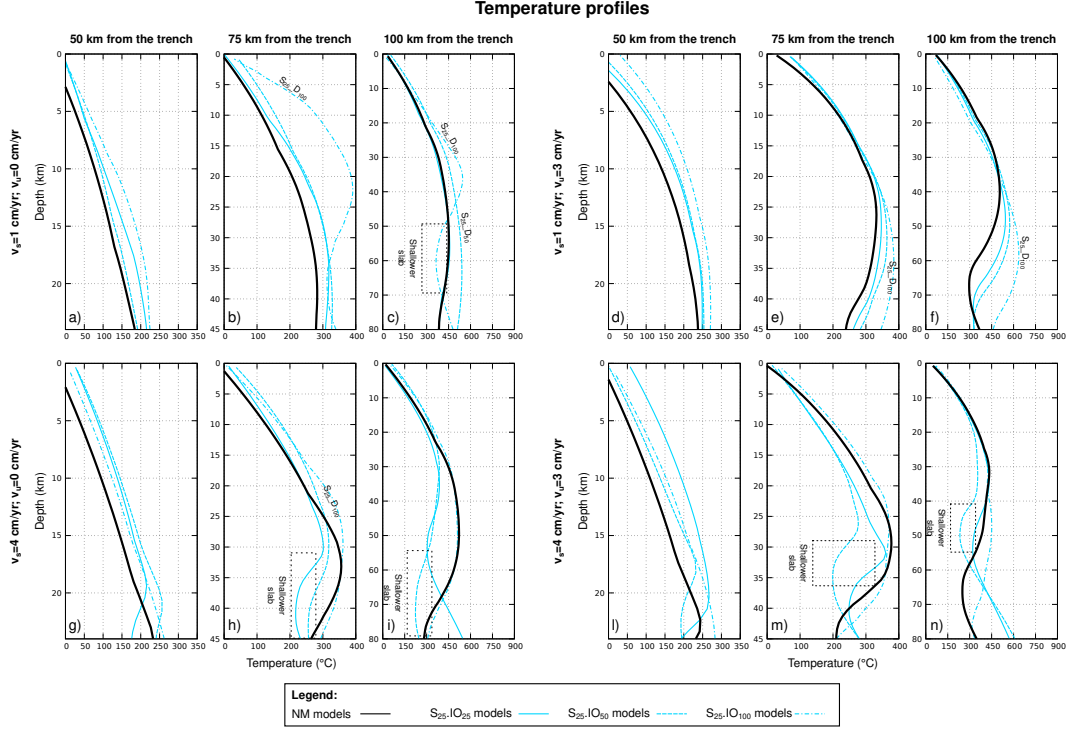
Figure 4. Temperature profiles for models with 25 km-wide microcontinent at different distances from the trench: 50 km (panels a, d, g, and l), 75 km (panels b, e, h, and m), and 100 km (panels c, f, i and, n). Continuous black lines indicate the profiles of models without microcontinents (NM). Continuous cyan lines indicate models with 25 km-wide inner ocean, dashed lines indicate models with 50 km-wide inner ocean, and dashed-dotted lines indicate models with 100 km-wide inner ocean.

between the plates, as previously observed in models NM3 and NM4. However, the recycling of material in these models occurs farther from the trench than in model S1 and beneath a thicker crust. This allows exhumation from a depth of 80 km up to approximately 40 km but not shallower (Fig. 3c and d). Consequently, the evolution of the topography is also similar to that observed in models without a microcontinent (models NM3 and NM4), because of the slight effects of the exhumed material (Fig. 3g and h).

The recycling of subducted material in the external portion of the mantle wedge weakens the mantle flux, as evidenced by the isotherm at 500 °C, which is farther from the trench in the wedge area compared to models NM3 and NM4 (compare continuous and dashed isotherms in Fig. 3c and d). The diminished mantle flux results in a less steep slab, with a decrease in the slab dip angle from 28° to 22° for models with a fixed upper plate (models NM3 and S3, respectively) and from 26° to 21° for models with $v_u = 3 \, \mathrm{cm \, yr^{-1}}$ (models NM4 and S4, respectively; observe differences between continuous and dashed isotherms in Fig. 3c and d). As a consequence, the temperature in the mantle wedge at 75 and 100 km from the trench decreases compared to NM models (continuous light blue lines in Fig. 4h, i, m, and n). In contrast, there is an increase of 50-100 °C in the temperatures in the most internal portion of the wedge (continuous light blue lines in Fig. 4g and l), as observed in the previous models.

3.2.2 *Effects of wider inner oceans - models S5-S12*

The increase in the dimension of the inner ocean (50 and 100 km, models S5-S12) does not significantly impact the thermo-mechanical evolution of the models. In the first half of the simulation, the topography evolution follows a pattern similar to that of the previous models, featuring an initial advancement (red stars in Fig. 5d and e) followed by a lesser retreat. On the contrary, a larger inner ocean generates a well-developed and lubricated subduction channel that facilitates the subduction of the microcontinent. Model $S5_{25}.IO_{50}.vs_1.vu_0$ is characterized by a steeper slab dip compared to models NM1 and S1, resulting in a warmer geotherm within the mantle wedge (Fig. 4a, b, c).

In model $S9_{25}.IO_{100}.vs_1.vu_0$, the microcontinent's initial location, farther from the upper plate, ensures that when it collides, the subduction channel is already fully developed. Consequently, its collision leads to a slight advancement of the trench after approximately 15 million years of evolution (pink star in Fig. 5e), not observed in previous models. Afterward, the trench remains stable for a few million years, until the exhumation of a substantial amount of subducted material causes an advancement of the accretionary wedge toward the subducting plate, resulting in a subsequent retreat of the trench (yellow star in Fig. 5e). Unlike other models, the S9 model still allows for easy subduction of the microcontinent, but the presence of a large amount of serpentinized crust related to a 100 km-wide inner ocean induces the exhumation of abundant subducted material from approximately 140 km depth up to the surface (Fig. 5b and Movie S4 in the Supporting Information). As a consequence, a more gentle slab dip occurs compared to models NM1, decreasing from 28° to 21° (dashed and continuous black lines, respectively, in Fig. 5b), and there is an increase in temperature by up to 150-200 °C in the central part of the mantle wedge compared to model S1. This difference is clearly visible when comparing geotherm75 and geotherm100 (dotted-dashed light blue lines in Fig. 4b and c).

A 100 km-wide inner ocean does not have any effect on models $S10_{25}.IO_{100}.vs_1.vu_3$ and $S12_{25}.IO_{100}.vs_4.vu_3$, while a few differences can be observed in model $S11_{25}.IO_{100}.vs_4.vu_0$. Specifically, unlike model S3, which showed a temperature decrease in the mantle wedge, model S11 is characterized by an increase in temperature of approximately 50 °C compared to the model without the microcontinent (dashed-dotted light blue and continuous black lines in Fig. 4h). In fact, unlike model S3, this model exhibits a slab dip an-
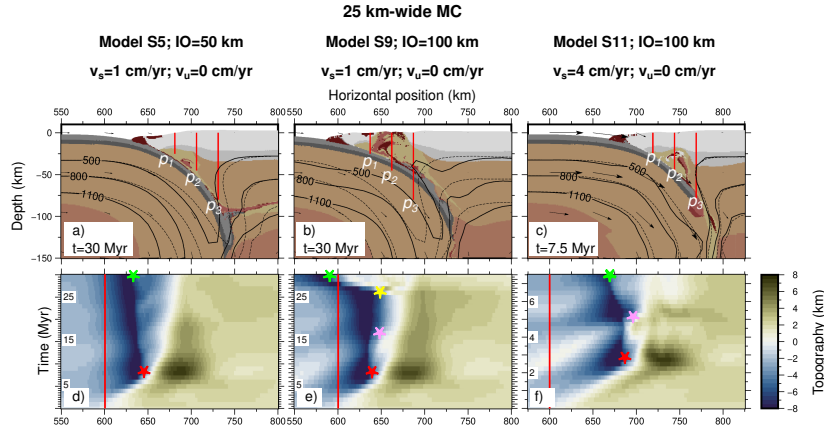
Figure 5. The evolution of models with a 25 km-wide microcontinent (MC) and 50 (panel a) and 100 (panels b and c) km-wide inner ocean (IO), including velocity fields, and the evolution of topography throughout the entire duration of simulations (panels d-f) are presented for different velocities of the subducting plate (v_s) and the upper plate (v_u). Red lines on panels a-c (p_1, p_2, and p_3) indicate the position of the thermal profiles shown in Fig. 4. Black lines indicate 500, 800 and 1100 °C isotherms, while dashed black lines indicate the same isotherms referred to NM models. Background colors define the composition as in Fig. 1. In panels d-f, red lines and red stars indicate the initial position and the maximum advancement of the trench, respectively, while the green stars indicate the maximum retreat of the trench. Pink stars indicate the collision of the microcontinent and yellow star indicates the beginning of exhumation of subducted material.

gle similar to model NM3 (see isotherm in Fig. 5c), and in this case, the recycling of continental material in the mantle wedge can contribute to a temperature increase.

On the contrary, the upwelling of subducted crust is not intense enough to provoke a trench retreat, as observed in models S1 and S9. The final retreat (green star in Fig. 5f) is due to the collapse of the topography of the upper plate, similar to model NM3. Nonetheless, the total retreat is less than in models NM3 because the collision and subsequent subduction of the microcontinent result in a temporary advancement of the trench after 5 million years (pink star in Fig. 5f).

3.3 Models with 50 km-wide microcontinent - models M

3.3.1 Models with 25 km-wide inner ocean - models M1-M4

The introduction of a larger microcontinent (MC=50 km) in the case of a small inner ocean (IO=25 km; models M1-M4) induces high coupling between the plates when the microcontinent collides. In models with a low velocity of the subducting plate ($M1_{50}.IO_{25}.vs_1.vu_0$ and $M2_{50}.IO_{25}.vs_1.vu_3$), this results in the accretion of the microcontinent at the trench, a jump of subduction backward (from s_1 to s_2 in Fig. 6a and b and Movies S5 in the Supporting Information), and subsequent detachment between the upper and lower continental crust, the latter being subducted. A forced trench retreat is thus observed (just after the red stars in Fig. 6i and l). However, the development of the new subduction channel (s_2 in Fig. 6a and b) occurs while the original channel is still active (s_1 in Fig. 6a and b), and, therefore, subduction is continuous throughout the entire evolution of these models.

Differently, the higher coupling observed in models with high velocities of the subducting plate (models M3 and M4) results in a temporary interruption of the subduction (approximately 0.5 Myr) after the collision of the microcontinent (models $M3_{50}.IO_{25}.vs_4.vu_0$ and $M4_{50}.IO_{25}.vs_4.vu_3$ in Fig. 6c and d). As a consequence, the strain rates in the shallowest part of the subduction channel decrease, and a back thrust fault develops behind the accretionary wedge (b_1 in Fig. 6c and d and Movie S6 in the Supporting Information). After that, the subduction restarts along a new subduction channel backward of the microcontinent (s_2 in Fig. 6c and d), with the detachment of the lower crust of the microcontinent and its subsequent subduction (Fig. 6g and h and Movie S7 in the Supporting Information). Since models M1, M2, M3 and M4 are characterized by the subduction of a small part of the microcontinent (primarily the lower crust), the recycling of subducted material in the mantle wedge is very limited (Fig. 6e-h).

From a thermal point of view, models M2, M3 and M4 are characterized by both a slight warming of approximately 25-50 °C in the most internal portion of the wedge (red continuous lines in Fig. 7d, l, and g) and a cooling of up to 100-150 °C along more external profiles (red continuous lines in Fig. 7e, f, h, i, n, and m) compared to the models without a microcontinent. The slight warming is attributed to the limited amount of crustal material recycled in the mantle wedge. On the contrary, the significant cooling in the external part of the mantle wedge is attributed to the shallow slab (slab dip of 21°) resulting from the collision of the microcontinent and the restart of subduction backward (Fig. 6g, h). On the contrary, model M1 shows no differences compared to model NM1 because the low velocities imposed at the boundaries result in a low global mantle flow. Therefore, the presence of limited amount of continental material has only a slight effect on the mantle flow inside the wedge (see isotherms in Fig. 6e).

3.3.2 Effects of wider inner oceans - models M5-M12

The increase in the dimension of the inner ocean to 50 km does not significantly affect the subduction dynamics compared to the models with a smaller inner ocean, except for model $M6_{50}.IO_{50}.vs_1.vu_3$, which does not exhibit a subduction jump at sur-
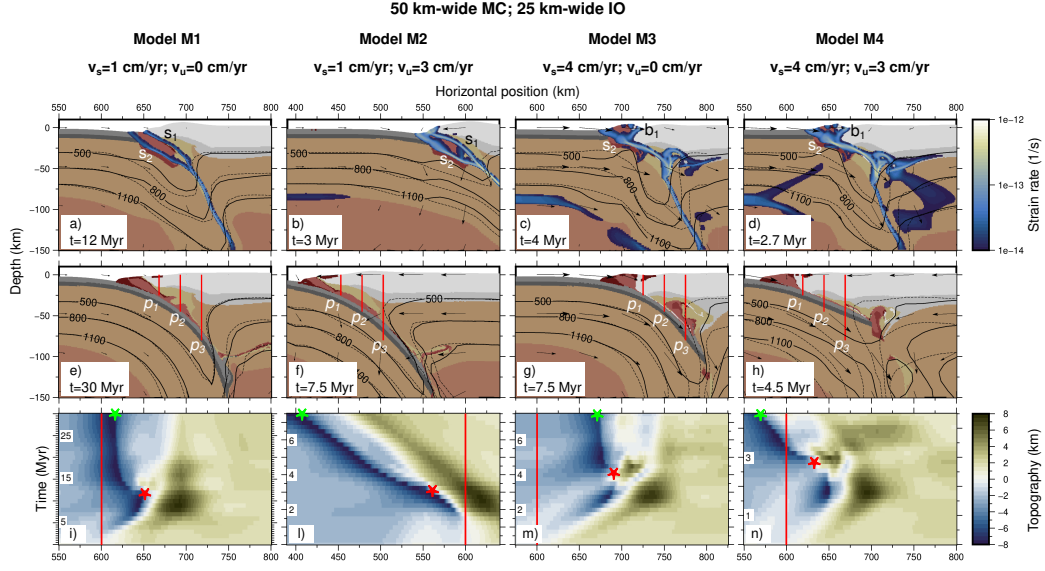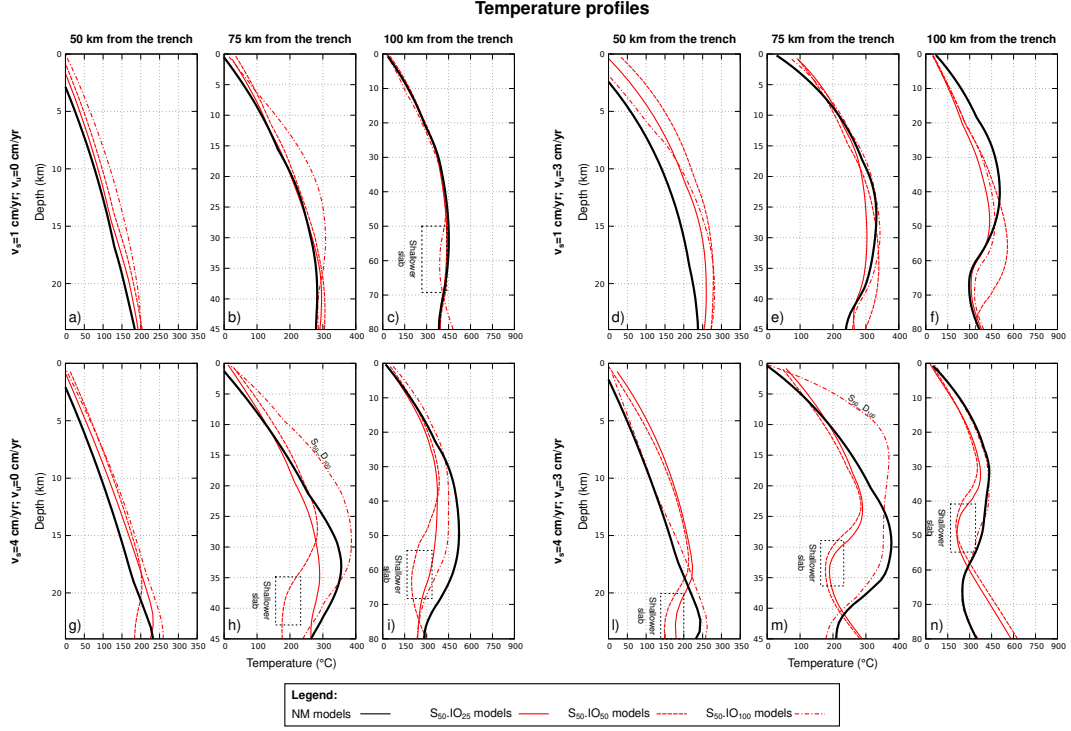
Figure 6. The evolution of models with a 50 km-wide microcontinent (MC) and a 25 km-wide inner ocean (IO) at two distinct stages, including velocity fields and strain rates (panels a-h), and the evolution of topography throughout the entire duration of simulations (panels i-n) are presented for different velocities of the subducting plate (v_s) and the upper plate (v_u). Red lines on panels a-d (p_1, p_2, and p_3) indicate the position of the thermal profiles shown in Fig. 7. s_1 indicates the first subduction channel and s_2 the second subduction channel after the subduction jump. b_1 indicates the back thrust fault inside the accretionary wedge. Black lines indicate 500, 800 and 1100 °C isotherms, while dashed black lines indicate the same isotherms referred to NM models. Background colors define the composition as in Fig. 1. In panels i-n, red lines and red stars indicate the initial position and the maximum advancement of the trench, respectively, while the green stars indicate the maximum retreat of the trench.

Figure 7. Temperature profiles for models with 50 km-wide microcontinent at different distances from the trench: 50 km (panels a, d, g, and l), 75 km (panels b, e, h, and m), and 100 km (panels c, f, i and, n). Continuous black lines indicate the profiles of models without microcontinents (NM). Continuous red lines indicate models with 25 km-wide inner ocean, dashed lines indicate models with 50 km-wide inner ocean, and dashed-dotted lines indicate models with 100 km-wide inner ocean.

Figure 8. The evolution of models with a 50 km-wide microcontinent (MC), 50 (panels a and e) and 100 (panels b-d and f-h) km-wide inner ocean (IO), at two distinct stages, including velocity fields and strain rates, and the evolution of topography throughout the entire duration of simulations (panels i-n) are presented for different velocities of the subducting plate (v_s) and the upper plate (v_u). Red lines on panels a-d (p_1, p_2, and p_3) indicate the position of the thermal profiles shown in Fig. 7. s_1 indicates the first subduction channel and s_2 the second subduction channel after the subduction jump. Black lines indicate 500, 800 and 1100 °C isotherms, while dashed black lines indicate the same isotherms referred to NM models. Background colors define the composition as in Fig. 1. In panels i-n, red lines and red stars indicate the initial position and the maximum advancement of the trench, respectively, while the green stars indicate the maximum retreat of the trench.

face. Instead, the detachment between the upper and lower continental crust of the microcontinent occurs deep in the subduction channel (from s_1 to s_2 in Fig. 8a and Movie S8 in the Supporting Information). However, the detachment occurs when the microcontinent is still shallow and, as a consequence, the larger amount of continental material in the inner portion of the wedge (Fig. 8e) determines the increases of temperature by up to 100°C due to the higher radiogenic energy produced (dashed red line in Fig. 7d). On the contrary, the increase in temperatures in the deeper and farther portion of the mantle wedge (7e and f) is attributed to the steep slab, compared to models without a microcontinent.

Conversely, an inner ocean of 100 km allows for more continuous subduction for all velocities considered (M9-M12 in Fig. 8b, c and d), without accretion of the microcontinent at the trench (Fig. 8f, g and h). Models $M9_{50}.IO_{100}.vs_1.vu_0$ and $M10_{50}.IO_{100}.vs_1.vu_3$ exhibit a similar behavior, characterized by the detachment between the upper and lower continental crust of the microcontinent deep in the subduction channel (from s_1 to s_2 in Fig. 8b and c), favoring the recycling and exhumation of subducted material from the microcontinent at the end of the evolution (Fig. 8f and g).

However, model M9 is characterized by a larger amount of recycled material due to the slower velocities in the mantle wedge, allowing for a wider area in which subducted material can be exhumed. Specifically, in model M9, there is exhumation up to 75 km

from the trench (profile p_2 in Fig. 8f), while in model M10, the recycling is limited to 50 km from the trench (profile p_1 in Fig. 8g). As a result, model M9 shows a higher temperature increase (approximately 80 °C) along geotherm75 (dotted-dashed red line in Fig. 7b), whereas model M10 is characterized by a similar increase in temperatures along geotherm50 (dotted-dashed red lines in Fig. 7d) and a decrease in temperature along geotherm100, as observed in models with a narrower inner ocean (red lines in Fig. 7f).

The push of the exhumed material against the accretionary wedge causes a sudden retreat of the trench, more noticeable in model M9, due to the larger amount of exhumed microcontinent (red stars in Fig. 8l and m). A similar behavior can also be observed by comparing models $M11_{50}.IO_{100}.vs_4.vu_0$ and $M12_{50}.IO_{100}.vs_4.vu_3$. Both models are characterized by the final upwelling of subducted material between 75 and 100 km from the trench (Fig. 8h), resulting in a remarkable temperature increase of approximately 100 °C along geotherm$_{75}$ (dotted-dashed red lines in Fig. 7h and m). The only difference is observed at the trench before the collision of the microcontinent, where model M11 shows a jump of the subduction in front of the microcontinent (from s_1 to s_2 in Fig. 8d, red star in Fig. 8n and Movie S9 in the Supporting Information), while model M12 displays a continuous subduction.

3.4 Models with 75 km-wide microcontinent - models L

3.4.1 Models with 25 km-wide inner ocean - models L1-L4

The introduction of a 75 km-wide microcontinent relatively close to the upper plate (25 km-wide inner ocean) does not significantly impact the evolution of models with low velocity of the subducting plate ($L1_{75}.IO_{25}.vs_1.vu_0$ and $L2_{75}.IO_{25}.vs_1.vu_3$) compared to models with smaller microcontinents (M1 and M2). In these models, there is still a jump of the subduction inside the microcontinent, resulting in the accretion of part of the microcontinent at the trench and limited recycling at the end of the evolution of the previously subducted portion of the microcontinent.

On the contrary, models with a faster upper plate (models $L3_{75}.IO_{25}.vs_4.vu_0$ and $L4_{75}.IO_{25}.vs_4.vu_3$) exhibit higher resistance to the subduction of the microcontinent compared to models with the same subduction velocity but smaller microcontinents (M3 and M4). In particular, model L3 is characterized by the interruption of the subduction associated with the development of a back thrust fault behind the accretionary wedge (s_1 and b_1 in Fig. 9a, respectively). However, unlike model M3, the subduction does not restart along a new subduction channel, and the final setting resembles that of a typical continental collision (Fig. 9c and Movie S10 in the Supporting Information). As a consequence, the topography does not feature a deep and narrow trench, and the oceanic basin advances continuously throughout the evolution (Fig. 9e).

Similarly, the initial phase of the evolution of model L4 resembles that of model M4, both characterized by the interruption of subduction and the development of a back thrust fault (b_1 in Fig. 9b and model M4 in Fig. 6d). However, in this case, the interruption of subduction lasts longer, and the development of a new subduction that separates the microcontinent (s_2 in Fig. 9b) occurs with a 1 Myr delay compared to M4, resulting in a more prolonged period of inactive subduction (Fig. 9f and Movie S11 in the Supporting Information). Nonetheless, the final configuration is very similar between models M4 and L4, both mechanically (compare Fig. 6g and Fig. 9d) and thermally (compare continuous red and yellow lines in Fig. 10l-n).

3.4.2 Effects of wider inner oceans - models L5-L12

For these models, an inner ocean of 50 km allows the subduction of the microcontinent only in the case of high subduction velocity and a fixed upper plate (model $L7_{75}.IO_{50}.vs_4.vu_0$), while no significant differences can be observed for all the other velocities considered. In
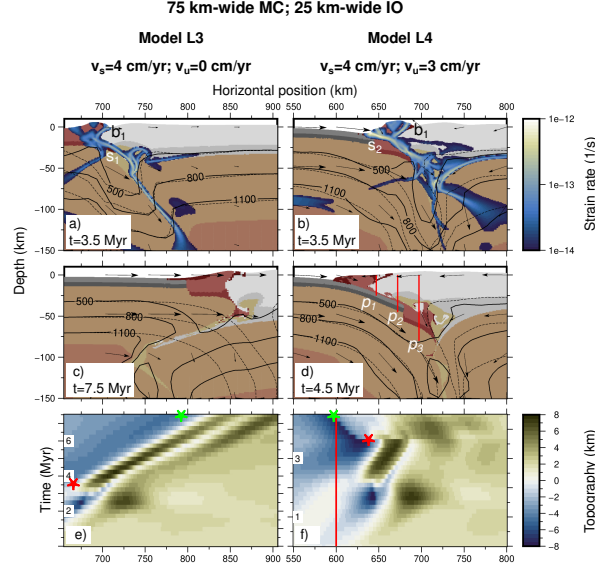
Figure 9. The evolution of models with a 75 km-wide microcontinent (MC) and a 25 km-wide inner ocean (IO) at two distinct stages, including velocity fields and strain rates (panels a-d), and the evolution of topography throughout the entire duration of simulations (panels e and f) are presented for different velocities of the subducting plate (v_s) and the upper plate (v_u). Red lines on panels d (p_1, p_2, and p_3) indicate the position of the thermal profiles shown in Fig. 10. s_1 indicates the first subduction channel and s_2 the second subduction channel after the subduction jump. b_1 indicates the back thrust fault inside the accretionary wedge. Black lines indicate 500, 800 and 1100 °C isotherms, while dashed black lines indicate the same isotherms referred to NM models. Background colors define the composition as in Fig. 1. In panels e and f, red lines and red stars indicate the initial position and the maximum advancement of the trench, respectively, while the green stars indicate the maximum retreat of the trench.

Figure 10. Temperature profiles at different distances from the trench: 50 km (panels a, d, g, and l), 75 km (panels b, e, h, and m), and 100 km (panels c, f, i and, n). Continuous black lines indicate the profiles of models without microcontinents (NM). Yellow lines indicate models with 75 km-wide microcontinent and dark green lines indicate models with 100 km-wide microcontinent. Continuous colored lines indicate models with 25 km-wide inner ocean, dashed colored lines indicate models with 50 km-wide inner ocean, and dashed-dotted colored lines indicate models with 100 km-wide inner ocean.

particular, model L7 is still characterized by both the interruption of subduction and the development of a back thrust fault behind the accretionary wedge (s_1 and b_1, respectively, in Fig. 11a). However, in this case, subduction is able to restart inside the microcontinent after approximately 2 Myr, similar to that observed for model L4, and the final setting is characterized by the accretion at the trench of a part of the microcontinent (Fig. 11d). The long interruption of subduction does not allow the development of a long slab at the end of the evolution, making it impossible to observe recycling in the wedge or to thermally compare this model with the model without a microcontinent.

A wider inner ocean (100 km) does not clearly affect the evolution of models with a low velocity of the subducting plate (models $L9_{75}.IO_{100}.vs_1.vu_0$ and $L10_{75}.IO_{100}.vs_1.vu_3$), which, once again, show a jump of subduction backward of the microcontinent, with the consequent accretion of part of the microcontinent at the trench (see models M1 and M2 in Fig. 6a, b, e, and f). Conversely, models $L11_{75}.IO_{100}.vs_4.vu_0$ and $L12_{75}.IO_{100}.vs_4.vu_3$ are characterized by the continuous subduction of the microcontinent. Although the final setting of these two models is very similar, showing both no accretion and recycling of subducted material at approximately 75-100 km from the trench (between profiles p_2 and p_3 in Fig. 11e and f), the dynamics differs before the collision of the microcontinent. Model L11 is characterized by the jump of the subduction channel in front of the microcontinent (from s_1 to s_2 in Fig. 11b), while model L12 shows a continuous subduction channel throughout the entire evolution (s_1 in Fig. 11c). The upwelling of subducted continental material from a maximum depth of approximately 50-60 km determines both a slight trench retreat (seen between red and green stars in Fig. 11h and i) and an increase in temperature compared to models NM3 and NM4 along geotherm$_{75}$ (dashed-dotted yellow lines in Fig. 10h and m).

3.5 Models with 100 km-wide microcontinent - models XL

Models with a 100 km-wide microcontinent exhibit a similar evolution to those observed in models with a 75 km-wide microcontinent, despite the larger dimension allowing for a greater amount of accreted material at the trench and increased recycling of subducted material. For example, in model $XL1_{100}.IO_{25}.vs_1.vu_0$, we observe a jump in subduction (from s_1 to s_2 in Fig. 12a), similar to what is seen in models L1 and M1 (Fig. 6a and e). However, the larger microcontinent size allows for the accretion of a greater amount of material at the trench, and, simultaneously, recycling of subducted material can be observed from a greater depth, approximately 70 km (between profiles p_2 and p_3 in Fig. 12e and Movie S12 in the Supporting Information). A similar behavior is observed in model $XL2_{100}.IO_{25}.vs_1.vu_3$. In contrast, in models $XL3_{100}.IO_{25}.vs_4.vu_0$ and $XL4_{100}.IO_{25}.vs_4.vu_3$, subduction is interrupted after the collision of the microcontinent, similar to the observation in model L3 (Fig. 9a and c).

Similar to observations in models with 75 km-wide microcontinents, a wider inner ocean facilitates the subduction of the microcontinent. In models $XL7_{100}.IO_{50}.vs_4.vu_0$ and $XL8_{100}.IO_{50}.vs_4.vu_3$, after the collision of the microcontinent, the subduction restarts with the development of a new subduction channel just before the end of the evolution (s_1 in Fig. 12b and f). Lastly, a 100 km-wide inner ocean allows for a more continuous subduction after the collision of the microcontinent in models $XL11_{100}.IO_{100}.vs_4.vu_0$ and $XL12_{100}.IO_{100}.vs_4.vu_3$, with no observed accretion at the trench (Fig. 12g and h). However, model XL11 is characterized by a jump of the subduction channel in front of the microcontinent, (from s_1 to s_2 in Fig. 12c), while model XL12 shows a continuous subduction throughout the entire evolution (s_1 in Fig. 12d). In these models, the subduction of the entire microcontinent results in the recycling of continental material between 75 and 100 far from the trench, from a depth of approximately 50 km (between profiles p_2 and p_3 in Fig. 12g and h). The upwelling of material determines an increase in temperature of the mantle wedge with respect to model without microcontinent, in particular along the geotherm$_{75}$ of model XL11 (dashed-dotted green line in Fig. 10h)
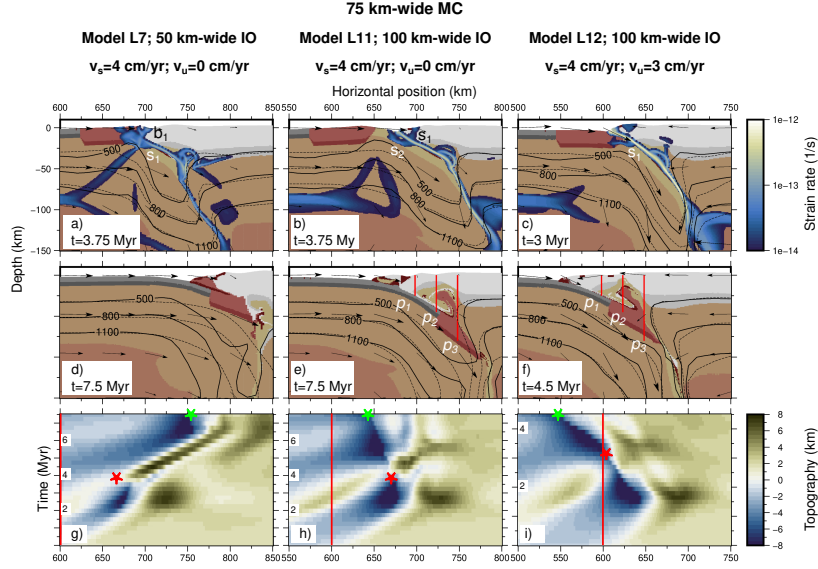
Figure 11. The evolution of models with a 75 km-wide microcontinent (MC) and a 50 (panels a and d) and 100 (panels b-c and e-f) km-wide inner ocean (IO) at two distinct stages, including velocity fields and strain rates (panels a-f), and the evolution of topography throughout the entire duration of simulations (panels g-i) are presented for different velocities of the subducting plate (v_s) and the upper plate (v_u). Red lines on panels a-d (p_1, p_2, and p_3) indicate the position of the thermal profiles shown in Fig. 10. s_1 indicates the first subduction zone and s_2 the second subduction zone after the subduction jump. b_1 indicates the back thrust fault inside the accretionary wedge. Black lines indicate 500, 800 and 1100 °C isotherms, while dashed black lines indicate the same isotherms referred to NM models. Background colors define the composition as in Fig. 1. In panels g-i, red lines and red stars indicate the initial position and the maximum advancement of the trench, respectively, while the green stars indicate the maximum retreat of the trench.

Figure 12. The evolution of models with a 100 km-wide microcontinent (MC) and a 25 (panels a and e), 50 (panels b and f), and 100 (panels c, d, g and h) km-wide inner ocean (IO) at two distinct stages, including velocity fields and strain rates are presented for different velocities of the subducting plate (v_s) and the upper plate (v_u). Red lines on panels e-d (p_1, p_2, and p_3) indicate the position of the thermal profiles shown in Fig. 10. s_1 indicates the first subduction zone and s_2 the second subduction zone after the subduction jump. Black lines indicate 500, 800 and 1100 °C isotherms, while dashed black lines indicate the same isotherms referred to NM models. Background colors define the composition as in Fig. 1.

and along all the geotherms calculated for model XL12 (dashed-dotted green lines in Fig. 10l-n).

4 Discussion

In this section, we first discuss the effects of plate velocities on subduction systems without microcontinents. Subsequently, we delve into the results regarding the mechanical impact (including accretion/subduction, slab geometry, and recycling) of microcontinents with varying sizes. We aim to compare our findings with previous research while placing special emphasis on thermal effects and their potential implications for the metamorphic conditions of recycled material. Finally, we briefly discuss our results in the context of different geodynamic reconstructions.

4.1 Impact of plate velocities on subduction systems without microcontinents

The evolution of our reference model without a microcontinent and low convergence velocity (v_s=1 cm yr^{-1} and v_u=0 cm yr^{-1}) represents the typical progression of an ocean-continent subduction system. This system is characterized by the localization of high strain rates along the plate interface, eventually forming a continuous subduction channel from the surface to the asthenospheric mantle.

The low velocity imposed on the subducting plate does not lead to significant coupling between the plates, resulting in a lack of high strain rates within the continental crust of the upper plate. Consequently, its deformation is restricted to the development of topographical height after a few million years of evolution, which tends to collapse over time. Moreover, the low coupling between the plates results in a lack of ablation of continental material from the upper plate.

The increase in the convergence velocity induces different behaviors depending on the velocities imposed on both the subducting and upper plates. In fact, the model with total convergence of 4 cm yr^{-1} and a faster upper plate (v_s=1 cm yr^{-1} and v_u=3 cm yr^{-1}) has a similar evolution of the model with v_s=1 cm yr^{-1} and the fixed upper plate, being characterized by low strain rates in the upper plate and lack of ablation.

On the contrary, the model with the same total convergence but with the entire velocity imposed on the subducting plate (v_s=4 cm yr^{-1} and v_u=0 cm yr^{-1}) shows higher coupling between the plates. This results in the development of both high strain rate bands and increased topography in the upper plate. Additionally, this model displays ablation of continental material from both the upper and lower crusts of the upper plate, leading to recycling in the mantle wedge. A similar behavior is observed when increasing the velocity of the upper plate in the case of a total convergence of 7cm yr^{-1}.

Therefore, our models demonstrate that the overall evolution of a subduction system is primarily controlled by the velocity of the subducting plate, leading to increased deformation of the upper plate at higher velocities. In contrast, different velocities of the upper plate have secondary effects on the evolution.

This finding is significant in the context of geodynamic reconstructions, where numerical simulations typically involve velocities imposed only on the subducting plate to replicate the total convergence between plates. However, our results indicate that the large-scale dynamics of subduction systems are not solely influenced by the total convergence velocity but also by the distribution of velocities on the two plates, even when the total convergence velocities are the same.

4.2 Impact of microcontinents on an ocean-continent subduction system

4.2.1 Type of subduction

We analyzed whether the presence of microcontinents with varying dimensions, situated at different distances from the trench, impacts the evolution of an ocean-continent subduction system. Our models indicate that predicting the subduction occurrence and patterns of microcontinents is challenging, as they depend on multiple factors that cannot be known a priori. However, general trends can be identified concerning the dimensions of both the microcontinent and the inner ocean, as well as the velocities of both the subducting and upper plates.

Our results indicate that continuous subduction can occur regardless of both the plate velocities and the inner ocean dimension, as long as small microcontinents are considered (i.e., 25 km; bottom row of Fig. 13). Consequently, none of these models exhibit accretion of continental material at the trench. Therefore, the accretionary wedge is formed solely by sediments produced at the trench.

On the contrary, the behavior of a subduction system in case of larger microcontinents (>25 km) depends both on the plate velocities and the dimension of the inner ocean. In general, an inner ocean larger than the microcontinent favors the development of a continuous subduction, often characterized by subduction of crustal material without accretion (green and yellow squares without 'A' in Fig. 13). However, a distinct difference is observed between models with low (v_s=1 cm yr^{-1}) and high (v_s=4 cm yr^{-1}) velocities of the subducting plate. Models with a low subducting plate velocity (v_s=1 cm yr^{-1}) are characterized by a continuous subduction, often with a jump in the subduction channel (yellow squares in Fig. 13). In fact, a continuous subduction can be observed only for models with 50 km-wide microcontinents and medium-large inner oceans (75-100 km), in relation to different velocities of the upper plate (green squares in Fig. 13). In contrast, models characterized either by 50 km-wide microcontinent and narrow
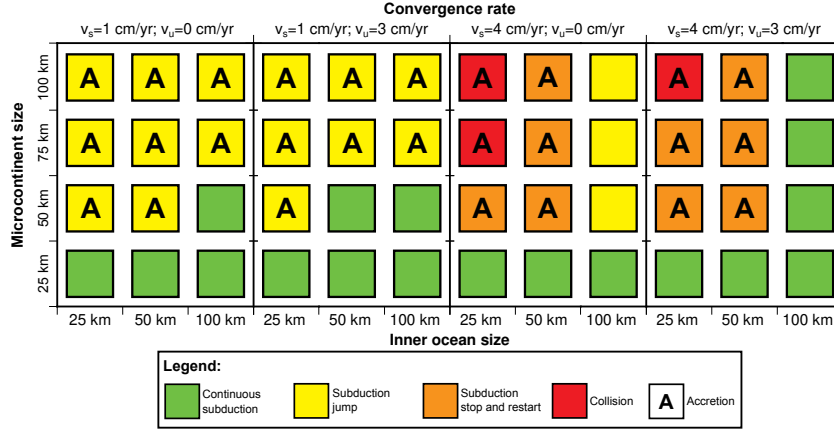
Figure 13. Different type of subduction observed. Green squares indicate models characterized by a continuous subduction; yellow squares indicate models in which the subduction is not interrupted but a jump of the subduction channel is observed; orange squares indicate models characterized by an interruption and a restart of the subduction along a new subduction channel; red squares indicate continental collision. Models with an 'A' are characterized by accretion of the microcontinent at the trench.

inner oceans, or by 75 and 100 km-wide microcontinent always show a jump in the subduction channel ('A' yellow squares in the top two lines of $v_s=1$ cm yr^{-1} models in Fig. 13). The jump of the channel occurs behind the microcontinent when the microcontinent has been partially subducted, leading to detachment between the upper and lower crust. This behavior promotes accretion at the trench of part of the upper crust of the microcontinent ('A' yellow squares in Fig. 13), while another part is recycled in the mantle wedge. However, recycling in these models is limited due to the small amount of subducted material.

Differently, models with $v_s=4$ cm yr^{-1} and 25-50 km-wide inner oceans show an interruption of the subduction when the microcontinents collide, with the consequent development of back thrust faults inside the upper plate (orange and red squares in Fig. 13). In most cases the subduction restarts along a new subduction channel locate within the microcontinent, with consequent accretion of the microcontinent at the trench ('A' orange squares in Fig. 13) and partial subduction and recycling of continental material. However, the restart does not occur in case of larger microcontinents and narrower inner oceans, and the models are characterized by a final setting typical of continental collision (red squares in Fig. 13), similar to what previously observed by Tao et al. (2020). Nonetheless, a 100 km-wide inner ocean eases the subduction, with differences related to the velocity of the upper plate. In fact, a continuous subduction without jump of the channel can be observed for $v_u=3$ cm yr^{-1} (green square in the last column in Fig. 13), while a subduction jump characterized the models with a fixed upper plate (yellow square without 'A' in Fig. 13). However, in this case the jump occurs before the collision of the microcontinent and the new subduction channel restart in front of it, therefore avoiding accretion of the microcontinent at the trench.

Therefore, our results show a direct dependence between the size of microcontinents, the size of the inner ocean, and the capability to be subducted or accreted. In general, a continuous subductions after the collision of the microcontinent does not occur if the microcontinent is wider than the size of the inner ocean, i.e. its distance from the trench. This correlation between size and initial distance of the microcontinent from the upper plate is in agreement with Yan et al. (2022), even if they considered larger microconti-

nents located further from the trench. In addition, higher velocities imposed on the subducting plates increase the coupling between the plates that results in greater difficulties to produce a continuous subduction or, in some cases, to subduct at all the microcontinent. On the contrary, higher velocities imposed on the upper plate ease the subduction of the microcontinent, as previously observed by Yang et al. (2018), and, in fact, all models with a 100 km-wide ocean and v_u=3 cm yr^{-1} are not characterized neither by interruption of the subduction nor jump of the subduction channel throughout their entire evolution.

All the various types of subduction we observed in our models (continuous subduction, jump of the subduction channel and collision) can be well compared to what observed in previous studies (Tetreault & Buiter, 2012; Vogt & Gerya, 2014; Yang et al., 2018), even if both different initial setup and different parameters for both rheology and initial boundary conditions were adopted. For example, either plateau subduction, underplating and basal accretion, or frontal accretion observed by Vogt and Gerya (2014) can be compared either to continuous subduction, jump of the subduction channel with both accretion and subduction, or collision of the microcontinent predicted by our models. Similarly, the evolution observed by Tetreault and Buiter (2012) in case of either homogeneous microcontinents or basal/middle detachment match either tha continuous subduction or the jump of the subduction channel noticed in our models.

In addition, the jump of the subduction channel has been hypothesized for geodynamic reconstructions in different convergent margins. For example, in the reconstruction of the evolution of the Sesia-Lanzo Zone in the western Alps, Babist et al. (2006) presented a kinematic model characterized by the collision of successive continental units (i.e., microcontinents) that resulted in accretion at the trench and retreat of the subduction channel behind the microcontinents. A similar behavior has been presented by Peng et al. (2022) in their reconstruction of the tectonic evolution of Central Tibet. They considered the collision of the microcontinent Amdo against Qiangtang, leading to the subsequent jump of the subduction behind Amdo.

4.2.2 Slab geometry

We examined the shallow slab dip (above 50 km depth) of all models to determine if it depends the investigated parameters. Our models revealed a correlation between the shallow slab dip and the presence and dimensions of the introduced microcontinents in the domain (Fig. 14). Specifically, we observed a linear decrease in the slab dip for wider microcontinents, with a linear correlation coefficient of r=-0.65 (indicated by the black line in Fig. 14), resulting in a variation of up to 10° between models with 25 km-wide and 100 km-wide microcontinents (Fig. 14). In contrast, the shallow slab dip does not appear to be directly correlated with either the dimensions of the inner ocean or the velocities of the plates, as already observed by Lallemand et al. (2005) and Roda et al. (2011).

On the contrary, the deep geometry of the slab seems unrelated to the size of the microcontinent but is closely tied to the velocities of the plates. All models exhibit a verticalization of the slab above 100 km deep, except for models with an upper plate moving faster than the subducting plate (v_s=1 cm yr^{-1} and v_u=3 cm yr^{-1}). For these models, two distinct behaviors can be observed: in the case of 25 or 50 km-wide microcontinents, the models are characterized by a horizontalization of the slab at approximately 200 km deep, while for larger microcontinents (i.e., 75 and 100 km), the slab does not exhibit any variation in slab dip.

4.2.3 Recycling in the mantle wedge

Different plate velocities influence the occurrence and style of crustal recycling in the mantle wedge, as illustrated in Fig. 15, where black arrows indicate whether recy-
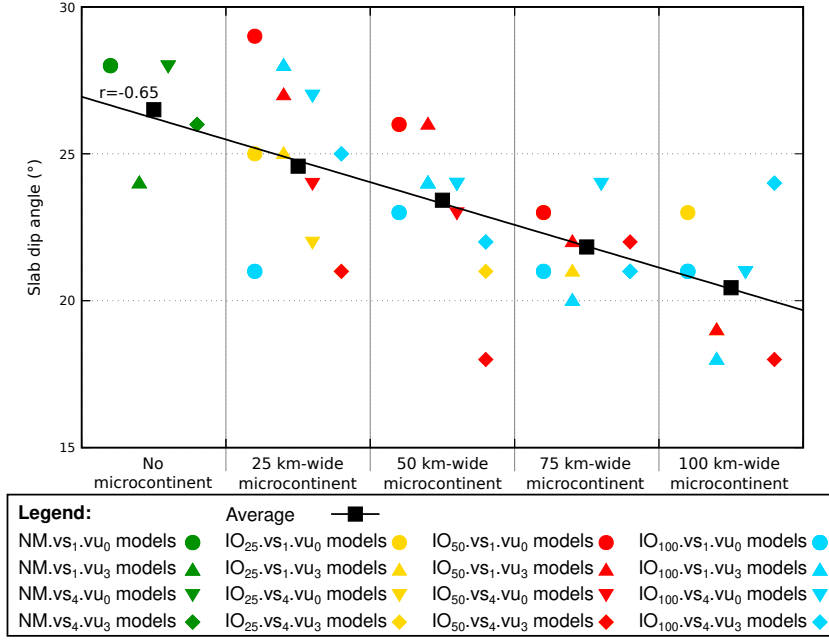
Figure 14. Shallow slab dip angle of all models in relation to the dimension of the microcontinent. Dark green indicate models without microcontinent; yellow, red and light blue indicate models with 25, 50 and 100 km-wide inner oceans, respectively. Different shapes indicate different velocities imposed on the plates. Black squares indicate the average dip for different dimension of the microcontinent and the black line represents the linear correlation.

cling of subducted material occurs for each model in different portions of the wedge at distances of 50, 75, and 100 km from the trench (left, central, and right colored rectangles). Our results indicate that models with high velocities of the upper plate (v_u=3 cm yr^{-1}) are characterized by either the absence or a small amount of recycled material, particularly when associated with a slow subducting plate (v_s=1 cm yr^{-1}). This is because the intense mantle flow below the overriding plate pushes the subducted material against the slab, preventing recycling. This behavior is more evident in models with 25 or 50 km-wide microcontinents, showing scarce or null recycling in the case of v_u=3 cm yr^{-1}, while abundant recycling is predicted at different distances for fixed upper plate (compare black arrows in the two bottom rows in Fig. 15). Furthermore, higher subducting velocities move the recycling area away from the trench. Models with v_s=1 cm yr^{-1} show recycling at 50/75 km from the trench (left/central colored rectangles of each model, respectively, in Fig. 15), while models characterized by faster subducting plates (v_s=4 cm yr^{-1}) exhibit recycling at 75/100 km from the trench (central/right colored rectangles of each model, respectively, in Fig. 15). A farther distance from the trench also results in deeper regions of recycling, making it more challenging to have upwelling up to the surface or even to shallow levels of the crust. Finally, large microcontinents (75-100 km) generally allow both a deep exhumation of the frontal portion of the microcontinent (from approximately 60-70 km deep) and a shallow exhumation of the central/back portion of the microcontinent (from approximately 15-20 km deep) in the case of v_s=1 cm yr^{-1}.

Therefore, the velocity of both plates and the size of a microcontinent are significant parameters to consider for better constraining geodynamic reconstruction in the case of exhumed rocks characterized by contrasting maximum pressure recorded. The recycling of subducted material also affects the dynamics of the trench. In fact, mod-
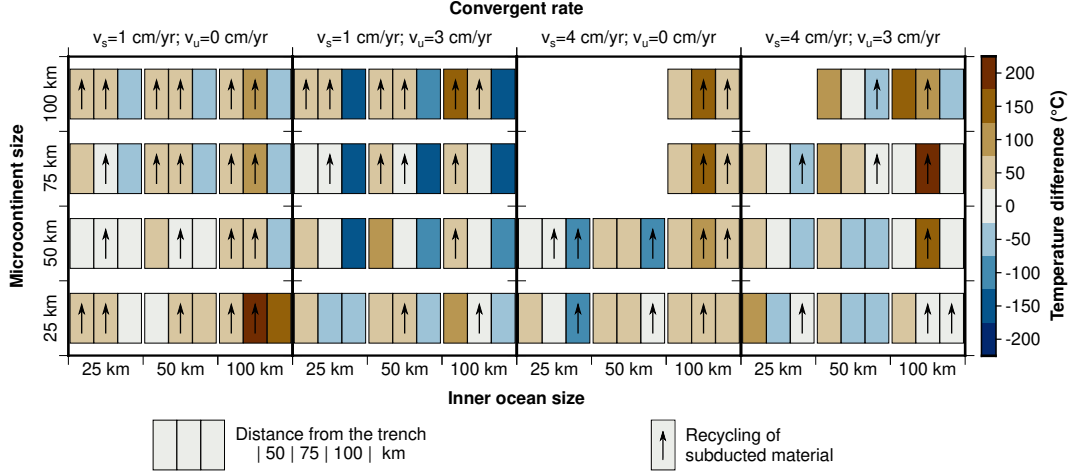
Figure 15. Temperature differences between each model and the equivalent models without microcontinent, calculated along geotherms located 50, 75 and 100 km far from the trench, as in Figs. 4, 7 and 10. Black arrows indicate areas characterized by exhumation of subducted material.

els with fast and abundant recycling are characterized by a clear trench retreat due to the push produced by the upwelling material toward the accretionary wedge.

4.2.4 Thermal effects

We discuss the thermal effects due to a microcontinent in the subduction system with respect to equivalent models without microcontinents by comparing the geotherms at three different distances from the trench (50, 75, and 100 km) to separate the mantle wedge into three regions: inner, central, and outer (Fig. 15).

Our results show that the introduction of a microcontinent in a subduction system has a clear impact on the thermal state recorded in the mantle wedge, with different effects observed in different regions of the mantle wedge (Fig. 15). In particular, the inner portion of the wedge shows a general warming compared to models without a microcontinent (red left rectangles in Fig. 15), while the central and outer portions are characterized either by warming or cooling (red or blue central/right rectangles in Fig. 15) as a result of different mechanical evolution of the system.

Since the recycling of material in the inner portion of the wedge (left rectangles in Fig. 15) is limited to shallow levels, the warming in this area (approximately 50-100 °C for all models; white/light red left rectangles in Fig. 15) can be related to the heat flux produced by the recycling of deep material pushing toward the trench. However, no additional heat can be related to higher radiogenic energy produced because the placement of continental crust from the microcontinent, either by accretion or by shallow recycling, replaces similar existing continental crust of the upper plate.

Differently, recycling of continental material in the central and outer portions of the mantle wedge produces warming related both to higher radiogenic energy, because of the large amount of continental crust in the mantle, and to upwelling of deeper and hotter material. Consequently, since the dynamic inside the mantle wedge is strictly correlated to plate velocities and the size and location of the microcontinent (as explained in Section 4.2.3), all of these factors affect the final thermal state of the models. Therefore, models characterized by parameters that favor the subduction of a larger amount

of continental material from the microcontinent (i.e., low velocities of the subducting plate or a large inner ocean) exhibit a warm central mantle wedge (up to 200 °C; central rectangles either in the left panel or in the last column of the third and fourth panels in Fig. 15), where the recycling, or even the exhumation up to the surface, is more abundant. Similarly, models with larger microcontinents are characterized by an increase in temperature up to 150-200 °C in the central portion of the wedge (dark red central rectangles in the top two lines in Fig. 15), when a large amount of continental crust is subducted (i.e., for a large inner ocean).

On the contrary, high velocity imposed on the upper plate determines less warming or even cooling of the mantle wedge (central rectangles in the central columns of the second and fourth panels in Fig. 15) because of low crustal recycling in the mantle wedge (as explained in Section 4.2.3). In addition, the recycling in the central and outer portions of the wedge, even if scarce, prevents the mantle flow below the overriding plate from reaching the mantle wedge, with a consequent lack of a significant source of heat. In fact, models with a more intense mantle flow (high velocities of the upper plate) are always characterized by cooling in the outer portion of the wedge, up to 150 °C (right blue rectangles in the second and fourth panels in Fig. 15). In addition, the thermal state in the most external portion of the wedge is also affected by the slab geometry because a higher slab dip facilitates a more intense counterflow in the mantle wedge that results in higher temperatures. Therefore, models with large microcontinents and high velocities of the upper plate further limit the mantle flow toward the wedge (as explained in Section 4.2.2 for the correlation between microcontinent size and slab dip).

The assessment of temperature variations in the mantle wedge is crucial to determining whether continental material recycled in the wedge records low or high temperatures. Consequently, the metamorphism recorded by these rocks may range from Lawsonite-bearing blueschist or eclogite facies conditions to HP granulites, depending on the microcontinent subduction setting. In general, we observed that recycling in the inner and central portions of the wedge is associated with a significant warming, reaching up to 150-200 °C. This warming is of great importance because the recycled material in these areas can be exhumed to the surface more easily. Therefore, the velocity of both plates and the size of microcontinents and inner oceans are significant parameters to consider, not only for their consequences on the mechanical evolution but also for their impact on the thermal state of the subduction system. These factors have direct effects on geodynamic reconstruction, especially in the case of exhumed rocks characterized by high temperatures recorded during active subduction.

4.3 Limitations and Future Works

In this work, we mainly focus on variations in the size and location of the microcontinent, as well as variations in the initial velocity boundary conditions imposed on both plates. We evaluate their effects on the evolution of subduction. However, we did not consider rheology variations for the different materials in this study. The effects of rheology variations and different thicknesses of the microcontinent have been previously analyzed in other works (e.g. Tetreault & Buiter, 2012; Vogt & Gerya, 2014), and they were proven to have effects on the subductibility of microcontinents.

Additionally, we did not consider either melting or hydration inside the mantle wedge, although both could have effects on the recycling of material and, therefore, on the final thermal setting of the models. Future studies could expand upon the work presented here by incorporating these aspects into the numerical code.

Similarly, we decided to use 2D models to explore in detail the effects of specific parameters throughout the entire evolution of subduction systems. However, future studies could include 3D numerical models to simulate more complex tectonic settings.

Finally, future works could involve a detailed analysis of pressure-temperature-time (PTt) paths predicted by the models for subducted and exhumed particles. This would allow for a comparison with natural PTt paths observed in systems thought to have experienced subduction and/or collision of microcontinents.

5 Conclusions

In this work, we investigated the effect of different velocities imposed on both plates on the evolution of an ocean-continent subduction system. In particular, we also analyzed whether the introduction of microcontinents, characterized by different sizes and initial distances from the trench, impacts the system's evolution.

The first significant result is that the dynamics of a subduction system, in the absence of microcontinents, are not only influenced by the total convergence velocity, but different velocities imposed on both plates, even with the same convergent velocity, also impact the evolution. In general, we observed that an increase in the velocity of the subducting plate leads to higher coupling between plates, resulting in the ablation of material from the upper plate, irrespective of the total convergence rate.

When microcontinents are introduced into the system, we observed four different styles of subduction that depend on the velocities of the plates and both the dimension and initial distance of the microcontinent from the upper plate. Specifically, our models showed: 1) continuous subduction, 2) continuous subduction with a jump in the subduction channel, 3) interruption and restart of the subduction along a new subduction channel, and 4) continental collision. We noticed that the subduction of microcontinents becomes more challenging as their dimensions increase, favoring the jump or interruption of subduction. On the contrary, a large inner ocean facilitates a continuous subduction. Additionally, different velocities of the plates also affect the subduction style; high subducting velocities make the subduction of microcontinents more difficult, while high velocities of the upper plate make it easier.

The style of subduction has primary effects on the wedge dynamics, particularly on the amount of subducted material that recycles in the mantle wedge, resulting in different thermal conditions. A fixed upper plate, especially if coupled with a slow subducting plate, favors the exhumation of recycled material from different depths up to either shallow levels or the surface. This is significant because the upwelling to shallow depths increases the temperature in the inner and central portions of the mantle wedge, directly affecting the metamorphic conditions recorded by subducted and exhumed rocks during their evolution.

Finally, models with conditions that favor the (partial) subduction of large microcontinents are characterized by synchronous exhumation of rocks derived from different portions of the microcontinent. Therefore, these rocks could have experienced either high or low-pressure and temperature conditions during their evolution.

Open Research Section

Acknowledgments

Author Contributions

Conceptualization - AR, MR; Formal analysis - AR; Investigation - AR; Methodology - AR, MR; Software - AR; Validation - AR, MR; Visualization - AR, MR; Writing - Original draft - AR, MR; Writing - Review & editing - AR, MR;

References

Abera, R., van Wijk, J., & Axen, G. (2016). Formation of continental fragments: The tamayo bank, gulf of california, mexico. *Geology*, *44*(8), 595–598. doi: 10.1130/g38123.1

Afonso, J. C., & Zlotnik, S. (2011). The subductability of continental lithosphere: The before and after story. *Frontiers in Earth Sciences*, *4*, 53–86. doi: 10.1007/978-3-540-88558-0_3

Alejano, L. R., & Bobet, A. (2012). Drucker-Prager criterion. *Rock Mechanics and Rock Engineering*, *45*(6), 995–999. doi: 10.1007/s00603-012-0278-2

Amestoy, P. R., Duff, I. S., L'Excellent, J.-Y., & Koster, J. (2001). A fully Asynchronous Multifrontal Solver using Distributed Dynamic Scheduling. *Society for Industrial and Applied Mathematics*, *23*(1), 15–41.

Amestoy, P. R., Guermouche, A., L'Excellent, J.-Y., & Pralet, S. (2006). Hybrid scheduling for the parallel solution of linear systems. *Parallel Computing*, *32*(2), 136–156. doi: 10.1016/j.parco.2005.07.004

Anderson, J. (1995). *Computational fluid dynamics*. McGraw-Hill.

Andrews, E. R., & Billen, M. I. (2009). Rheologic controls on the dynamics of slab detachment. *Tectonophysics*, *464*(1), 60–69. doi: 10.1016/j.tecto.2007.09.004

Arredondo, K. M., & Billen, M. I. (2016). The effects of phase transitions and compositional layering in two-dimensional kinematic models of subduction. *Journal of Geodynamics*. doi: 10.1016/j.jog.2016.05.009

Babeyko, A. Y., & Sobolev, S. V. (2005). Quantifying different modes of the late Cenozoic shortening in the central Andes. *Geology*, *33*(8), 621–624. doi: 10.1130/G21126.1

Babist, J., Handy, M. R., Konrad-Schmolke, M., & Hammerschmidt, K. (2006). Pre-collisional, multistage exhumation of subducted continental crust: The Sesia Zone, western Alps. *Tectonics*, *25*(TC6008). doi: 10.1029/2005TC001927

Billen, M. I., & Hirth, G. (2007). Rheologic controls on slab dynamics. *Geochem. Geophys. Geosyst.*, *8*(8). doi: 10.1029/2007GC001597

Bollino, A., Regorda, A., Sabadini, R., & Marotta, A. M. (2022). From rifting to oceanization in the Gulf of Aden: Insights from 2D numerical models. *Tectonophysics*, *838*, 229483. doi: 10.1016/j.tecto.2022.229483

Braun, J., & Willett, S. D. (2013). A very efficient o(n), implicit and parallel method to solve the stream power equation governing fluvial incision and landscape evolution. *Geomorphology*, *180-181*, 170-179. doi: 10.1016/j.geomorph.2012.10.008

Burov, E. B. (2011). Rheology and strength of the lithosphere. *Marine and Petroleum Geology*, *28*(8), 1402–1443. doi: 10.1016/j.marpetgeo.2011.05.008

Chopin, C. (1984). Coesite and pure pyrope in high-grade blue- schists of the Western Alps. *Contrib Mineral Petrol*, *86*, 107–118.

Chopin, C. (2003). Ultrahigh-pressure metamorphism: tracing continental crust into the mantle. *Earth and Planetary Science Letters*, *212*(1), 1-14. doi: 10.1016/S0012-821X(03)00261-9

Christensen, U. R., & Yuen, D. A. (1985). Layered convection induced by phase transitions. *Journal of Geophysical Research*, *90*(B12), 10291–10300. doi: 10.1029/JB090iB12p10291

Cloos, M. (1993). Lithospheric buoyancy and collisional orogenesis: Subduction of oceanic plateaus, continental margins, island arcs, spreading ridges, and seamounts. *Geological Society of America Bulletin*, *105*(6), 715. doi: 10.1130/0016-7606(1993)105⟨0715:LBACOS⟩2.3.CO;2

Cordonnier, G., Bovy, B., & Braun, J. (2019). A versatile, linear complexity algorithm for flow routing in topographies with depressions. *Earth Surface Dynamics*, *7*(2), 549–562. doi: 10.5194/esurf-7-549-2019

Crameri, F. (2018a). Geodynamic diagnostics, scientific visualisation and StagLab 3.0. *Geoscientific Model Development*, *11*(6), 2541–2562. doi: 10.5194/gmd-11

-2541-2018

Crameri, F. (2018b). *Scientific colour-maps.* Zenodo. doi: 10.5281/zenodo.1243862

Crameri, F., Magni, V., Domeier, M., Shephard, G. E., Chotalia, K., Cooper, G., . . . Thielmann, M. (2020). A transdisciplinary and community-driven database to unravel subduction zone initiation. *Nature Communications*, *11*, 3750. doi: 10.1038/s41467-020-17522-9

De Franco, R., Govers, R., & Wortel, R. (2008a). Dynamics of continental collision: influence of the plate contact. *Geophysical Journal International*, *174*(3), 1101–1120. doi: 10.1111/j.1365-246X.2008.03857.x

De Franco, R., Govers, R., & Wortel, R. (2008b). Nature of the plate contact and subduction zones diversity. *Earth and Planetary Science Letters*, *271*, 245–253. doi: 10.1016/j.epsl.2008.04.019

Donea, J., & Huerta, A. (2003). *Finite Element Methods for Flow Problems* (Vol. 1). Wiley. doi: 10.1017/CBO9781107415324.004

Donea, J., Huerta, A., Ponthot, J.-P., & Rodríguez-Ferran, A. (2004). Arbitrary Lagrangian–Eulerian Methods. In *Encyclopedia of computational mechanics* (chap. 14). John Wiley & Sons, Ltd. doi: 10.1002/0470091355.ecm009

Duretz, T., Gerya, T. V., & May, D. A. (2011). Numerical modelling of spontaneous slab breakoff and subsequent topographic response. *Tectonophysics*, *502*(1–2), 244–256. doi: 10.1016/j.tecto.2010.05.024

Ellis, S., Beaumont, C., & Pfiffner, O. A. (1999). Geodynamic models of crustal-scale episodic tectonic accretion and underplating in subduction zones. *Journal of Geophysical Research: Solid Earth*, *104*(B7), 15169-15190. doi: 10.1029/1999JB900071

Erdős, Z., Huismans, R. S., & van der Beek, P. (2019). Control of increased sedimentation on orogenic fold-and-thrust belt structure – insights into the evolution of the Western Alps. *Solid Earth*, *10*(2), 391–404. doi: 10.5194/se-10-391-2019

Gerya, T. V., Fossati, D., Cantieni, C., & Seward, D. (2009). Dynamic effects of aseismic ridge subduction: numerical modelling. *European Journal of Mineralogy*, *21*(3), 649–661. doi: 10.1127/0935-1221/2009/0021-1931

Gerya, T. V., & Stöckhert, B. (2002). Exhumation rates of high pressure metamorphic rocks in subduction channels: The effect of Rheology. *Geophysical Research Letters*, *29*(8), 1–19. doi: 10.1029/2002TC001406

Gerya, T. V., & Stöckhert, B. (2006). Two-dimensional numerical modeling of tectonic and metamorphic histories at active continental margins. *International Journal of Earth Sciences*, *90*(2), 250–274. doi: 10.1007/s00531-005-0035-9

Gerya, T. V., & Yuen, D. A. (2003). Rayleigh-Taylor instabilities from hydration and melting propel 'cold plumes' at subduction zones. *Earth and Planetary Science Letters*, *212*, 47–62. doi: 10.1016/S0012-821X(03)00265-6

Gerya, T. V., Yuen, D. A., & Maresch, W. V. (2004). Thermomechanical modelling of slab detachment. *Earth and Planetary Science Letters*, *226*, 101–116. doi: 10.1016/j.epsl.2004.07.02210.1016/j.epsl.2004.07.02210.1016/j.epsl.2004.07.022

Glerum, A., Thieulot, C., Fraters, M., Blom, C., & Spakman, W. (2018). Nonlinear viscoplasticity in ASPECT: Benchmarking and applications to subduction. *Solid Earth*, *9*(2), 267–294. doi: 10.5194/se-9-267-2018

Gün, E., Pysklywec, R. N., Göğüş, O. H., & Topuz, G. (2022). Terrane geodynamics: Evolution on the subduction conveyor from pre-collision to post-collision and implications on tethyan orogeny. *Gondwana Research*, *105*, 399-415. doi: 10.1016/j.gr.2021.09.018

Heuret, A., Funiciello, F., Faccenna, C., & Lallemand, S. (2007). Plate kinematics, slab shape and back-arc stress: A comparison between laboratory models and current subduction zones. *Earth and Planetary Science Letters*, *256*, 473–483. doi: 10.1016/j.epsl.2007.02.004

Hirth, G., & Kohlstedt, D. (2003). Rheology of the upper mantle and the mantle

wedge: A view from the experimentalists. In *Inside the subduction factory* (pp. 83–105). American Geophysical Union (AGU). doi: 10.1029/138GM06

Hughes, T. J. R., & Brooks, A. (1982). A theoretical framework for Petrov-Galerkin methods with discontinuous weighting functions: application to the streamline-upwind procedure. *Finite Elements in Fluids*, *4*, 47–65.

Huismans, R. S., & Beaumont, C. (2003). Symmetric and asymmetric lithospheric extension: Relative effects of frictional-plastic and viscous strain softening. *Journal of Geophysical Research: Solid Earth*, *108*(B10), 1–22. doi: 10.1029/2002JB002026

Huismans, R. S., Buiter, S. J. H., & Beaumont, C. (2005). Effect of plastic-viscous layering and strain softening on mode selection during lithospheric extension. *Journal of Geophysical Research: Solid Earth*, *110*(B2), 1–17. doi: 10.1029/2004JB003114

Ismail-Zadeh, A., & Tackley, P. J. (2010). *Computational Methods for Geodynamics*. New York: Cambridge University Press.

Jarrard, R. D. (1986). Relations Among Subduction Parameters. *Review of Geophysics*, *24*(2), 217–284.

Karato, S.-I. (2008). *Deformation of Earth Materials - An introduction to the rheology of solid Earth*. Cambridge University Press. doi: 10.1017/cbo9780511804892

Kaus, B. J. P., Mühlhaus, H., & May, D. A. (2010). A stabilization algorithm for geodynamic numerical simulations with a free surface. *Physics of the Earth and Planetary Interiors*. doi: 10.1016/j.pepi.2010.04.007

Koptev, A., Beniest, A., Gerya, T., Ehlers, T. A., Jolivet, L., & Leroy, S. (2019). Plume-induced breakup of a subducting plate: Microcontinent formation without cessation of the subduction process. *Geophysical Research Letters*, *46*(7), 3663-3675. doi: 10.1029/2018GL081295

Lallemand, S., Heuret, A., & Boutelier, D. (2005). On the relationships between slab dip, back-arc stress, upper plate absolute motion, and crustal nature in subduction zones. *Geochemistry Geophysics Geosystems*, *6*(9), 1–18. doi: 10.1029/2005GC000917

Le Pourhiet, L., May, D. A., Huille, L., Watremez, L., & Leroy, L. (2017). A genetic link between transform and hyper-extended margins. *Earth and Planetary Science Letters*, *465*, 184–192. doi: 10.1016/j.epsl.2017.02.043

Liu, L., Zhang, J., Green, H. W., Jin, Z., & Bozhilov, K. N. (2007). Evidence of former stishovite in metamorphosed sediments, implying subduction to ¿350 km. *Earth and Planetary Science Letters*, *263*(3), 180-191. doi: 10.1016/j.epsl.2007.08.010

Magni, V., Naliboff, J., Prada, M., & Gaina, C. (2021). Ridge jumps and mantle exhumation in back-arc basins. *Geosciences*, *11*(11), 475. doi: 10.3390/geosciences11110475

Marotta, A. M., Restelli, F., Bollino, A., Regorda, A., & Sabadini, R. (2020). The static and time-dependent signature of ocean–continent and ocean–ocean subduction: the case studies of Sumatra and Mariana complexes. *Geophysical Journal International*, *221*(2), 788–825. doi: 10.1093/gji/ggaa029

Marotta, A. M., Spelta, E., & Rizzetto, C. (2006). Gravity signature of crustal subduction inferred from numerical modelling. *Geophys. J. Int.*, *166*, 923–938. doi: 10.1111/j.1365-246X.2006.03058.x

Molnar, N. E., Cruden, A. R., & Betts, P. G. (2018). Unzipping continents and the birth of microcontinents. *Geology*, *46*(5), 451-454. doi: 10.1130/G40021.1

Müller, R. D., Gaina, C., Roest, W. R., & Hansen, D. L. (2001). A recipe for microcontinent formation. *Geology*, *29*(3), 203. doi: 10.1130/0091-7613(2001)029⟨0203:arfmf⟩2.0.co;2

Naliboff, J. B., & Buiter, S. J. H. (2015). Rift reactivation and migration during multiphase extension. *Earth and Planetary Science Letters*, *421*, 58–67. doi:

http://dx.doi.org/10.1016/j.epsl.2015.03.050

Naliboff, J. B., Glerum, A., Brune, S., Péron-Pinvidic, G., & Wrona, T. (2020). Development of 3-D Rift Heterogeneity Through Fault Network Evolution. *Geophysical Research Letters*, *47*(13), e2019GL086611. doi: 10.1029/2019GL086611

Nemčok, M., Sinha, S. T., Doré, A. G., Lundin, E. R., Mascle, J., & Rybár, S. (2016). Mechanisms of microcontinent release associated with wrenching-involved continental break-up: a review. *Geological Society, London, Special Publications*, *431*(1), 323–359. doi: 10.1144/sp431.14

O'Brien, P. J., Zotov, N., Law, R., Khan, M. A., & Jan, M. Q. (2001). Coesite in Himalayan eclogite and implications for models of India-Asia collision. *Geology*, *29*, 435–438. doi: 10.1130/0091-7613(2001)029⟨0435:CIHEAI⟩2.0.CO;2

Peng, Y., Yu, S., Li, S., Liu, Y., Santosh, M., Lv, P., ... Liu, Y. (2022). Tectonic erosion and deep subduction in central tibet: Evidence from the discovery of retrograde eclogites in the amdo microcontinent. *Journal of Metamorphic Geology*, *40*(9), 1545-1572. doi: 10.1111/jmg.12685

Péron-Pinvidic, G., & Manatschal, G. (2010). From microcontinents to extensional allochthons: witnesses of how continents rift and break apart? *Petroleum Geoscience*, *16*(3), 189–197. doi: 10.1144/1354-079309-903

Petersen, K. D., & Schiffer, C. (2016). Wilson cycle passive margins: Control of orogenic inheritance on continental breakup. *Gondwana Research*, *39*, 131–144. doi: 10.1016/j.gr.2016.06.012

Polino, R., Dal Piaz, G. V., & Gosso, G. (1990). Tectonic erosion at the Adria margin and accretionary processes for the Cretaceous orogeny of the Alps . *Mémoires de la Societé Géologique de France*, *156*, 345–367.

Quinquis, M. E. T., & Buiter, S. J. H. (2014). Testing the effects of basic numerical implementations of water migration on models of subduction dynamics. *Solid Earth*, *5*(1), 537–555. doi: 10.5194/se-5-537-2014

Ranalli, G. (1995). *Rheology of the Earth.* Springer Netherlands.

Regorda, A. (2022). *FALCON: a 2D numerical model.* Zenodo. doi: 10.5281/zenodo.7081225

Regorda, A., & Roda, M. (2023). *Microcontinent collision: input and dataset vtu files.* Zenodo. doi: 10.5281/zenodo.8304780

Regorda, A., Roda, M., Marotta, A. M., & Spalla, M. I. (2017). 2-D numerical study of hydrated wedge dynamics from subduction to post-collisional phases. *Geophysical Journal International*, *211*(2), 974–1000. doi: 10.1093/gji/ggx336

Regorda, A., Spalla, M. I., Roda, M., Lardeaux, J., & Marotta, A. M. (2021). Metamorphic Facies and Deformation Fabrics Diagnostic of Subduction: Insights From 2D Numerical Models. *Geochemistry, Geophysics, Geosystems*, *22*(10). doi: 10.1029/2021GC009899

Regorda, A., Thieulot, C., van Zelst, I., Erdős, Z., Maia, J., & Buiter, S. (2023). Rifting Venus: Insights From Numerical Modeling. *Journal of Geophysical Research: Planets*, *128*(3), e2022JE007588. doi: 10.1029/2022JE007588

Roda, M., Marotta, A. M., & Spalla, M. I. (2010). Numerical simulations of an ocean-continent convergent system: Influence of subduction geometry and mantle wedge hydration on crustal recycling. *Geochemistry Geophysics Geosystems*, *11*(5), 1–21. doi: 10.1029/2009GC003015

Roda, M., Marotta, A. M., & Spalla, M. I. (2011). The effects of the overriding plate thermal state on the slab dip in an ocean-continent subduction system. *Compte Rendu Academie des Sciences Paris*, *343*(5), 323–330. doi: 10.1016/j.crte.2011.01.005

Roda, M., Spalla, M. I., & Marotta, A. M. (2012). Integration of natural data within a numerical model of ablative subduction: a possible interpretation for the Alpine dynamics of the Austroalpine crust. *Journal of Metamorphic Geology*, *30*(9), 973–996. doi: 10.1111/jmg.12000

Rolf, T., Capitanio, F. A., & Tackley, P. J. (2018). Constraints on mantle viscosity structure from continental drift histories in spherical mantle convection models. *Tectonophysics*, *746*, 339–351. doi: 10.1016/j.tecto.2017.04.031

Rosenbaum, G., & Lister, G. S. (2005). The Western Alps from the Jurassic to Oligocene: spatio-temporal constraints and evolutionary reconstructions. *Earth-Science Reviews*, *69*, 281–306. doi: 10.1016/j.earscirev.2004.10.001

Salazar-Mora, C. A., Huismans, R. S., Fossen, H., & Egydio-Silva, M. (2018). The Wilson Cycle and Effects of Tectonic Structural Inheritance on Rifted Passive Margin Formation. *Tectonics*, *37*(9), 3085–3101. doi: 10.1029/2018TC004962

Schellart, W. P. (2005). Influence of the subducting plate velocity on the geometry of the slab and migration of the subduction hinge. *Earth and Planetary Science Letters*, *231*, 197–219. doi: 10.1016/j.epsl.2004.12.019

Scrutton, R. A. (1976). Microcontinents and their significance. In *Geodynamics: Progress and prospects* (p. 177-189). American Geophysical Union (AGU). doi: 10.1029/SP005p0177

Sinha, S. T., Nemčok, M., Choudhuri, M., Sinha, N., & Rao, D. P. (2015). The role of break-up localization in microcontinent separation along a strike-slip margin: the east india–elan bank case study. *Geological Society, London, Special Publications*, *431*(1), 95–123. doi: 10.1144/sp431.5

Smith, D. C. (1984). Coesite in clinopyroxene in the Caledonides and its implication for geodynamics. *Nature*, *310*, 641–644.

Sobolev, N. V., & Shatsky, V. S. (1990). Diamond inclusions in garnets from metamorphic rocks. *Nature*, *343*, 742–746.

Sobolev, S. V., & Babeyko, A. Y. (2005). What drives orogeny in the Andes? *Geology*, *33*(8), 617–620. doi: 10.1130/G21557.1

Spalla, M. I., Lardeaux, J.-M., Dal Piaz, G. V., Gosso, G., & Messiga, B. (1996). Tectonic significance of alpine eclogites. *Journal of Geodynamics*, *21*(3), 257–285. doi: 10.1016/0264-3707(95)00033-X

Stein, M., & Ben-Avraham, Z. (2007). Mechanisms of Continental Crust Growth. In G. Schubert (Ed.), *Treatise on geophysics* (pp. 171–195). Amsterdam: Elsevier. doi: 10.1016/B978-044452748-6.00144-9

Tao, J., Dai, L., Lou, D., Li, Z.-H., Zhou, S., Liu, Z., . . . Li, F. (2020). Accretion of oceanic plateaus at continental margins: Numerical modeling. *Gondwana Research*, *81*, 390-402. doi: 10.1016/j.gr.2019.11.015

Tetreault, J. L., & Buiter, S. J. H. (2012). Geodynamic models of terrane accretion: Testing the fate of island arcs, oceanic plateaus, and continental fragments in subduction zones. *Journal of Geophysical Research: Solid Earth*, *117*(B8). doi: 10.1029/2012JB009316

Tetreault, J. L., & Buiter, S. J. H. (2014). Future accreted terranes: a compilation of island arcs, oceanic plateaus, submarine ridges, seamounts, and continental fragments. *Solid Earth*, *5*(2), 1243–1275. doi: 10.5194/se-5-1243-2014

Theunissen, T., & Huismans, R. S. (2019). Long-Term Coupling and Feedback Between Tectonics and Surface Processes During Non-Volcanic Rifted Margin Formation. *Journal of Geophysical Research: Solid Earth*, *124*(11), 12323–12347. doi: 10.1029/2018JB017235

Thieulot, C. (2011). FANTOM: Two- and three-dimensional numerical modelling of creeping flows for the solution of geological problems. *Physics of the Earth and Planetary Interiors*, *188*(1-2), 47–68. doi: 10.1016/j.pepi.2011.06.011

Thieulot, C. (2014). ELEFANT: a user-friendly multipurpose geodynamics code. *Solid Earth Discussions*, *6*(2), 1949–2096. doi: 10.5194/sed-6-1949-2014

Thieulot, C., & Bangerth, W. (2022). On the choice of finite element for applications in geodynamics. *Solid Earth*, *13*(1), 229–249. doi: 10.5194/se-13-229-2022

van den Broek, J., & Gaina, C. (2020). Microcontinents and continental fragments associated with subduction systems. *Tectonics*, *39*(8), e2020TC006063. doi: 10.1029/2020TC006063

van den Broek, J., Magni, V., Gaina, C., & Buiter, S. (2020). The formation of continental fragments in subduction settings: The importance of structural inheritance and subduction system dynamics. *Journal of Geophysical Research: Solid Earth*, *125*(1), e2019JB018370. doi: 10.1029/2019JB018370

van Zelst, I., Crameri, F., Pusok, A. E., Glerum, A., Dannberg, J., & Thieulot, C. (2022). 101 geodynamic modelling: how to design, interpret, and communicate numerical studies of the solid Earth. *Solid Earth*, *13*(3), 583–637. doi: 10.5194/se-13-583-2022

Vogt, K., & Gerya, T. V. (2014). From oceanic plateaus to allochthonous terranes: Numerical modelling. *Gondwana Research*, *25*(2), 494–508. doi: 10.1016/j.gr.2012.11.002

Wang, H., Agrusta, R., & van Hunen, J. (2015). Advantages of a conservative velocity interpolation (CVI) scheme for particle-in-cell methods with application in geodynamic modeling. *Geochemistry, Geophysics, Geosystems*, *16*(6), 2015–2023. doi: 10.1002/2015GC005824

Wang, X., Liou, J. G., & Mao, H. K. (1989). Coesite-bearing eclogite from the dabie mountains in central china. *Geology*, *17*(12), 1085. doi: 10.1130/0091-7613(1989)017⟨1085:cbeftd⟩2.3.co;2

Warren, C. J., Beaumont, C., & Jamieson, R. A. (2008). Modelling tectonic styles and ultra-high pressure (UHP) rock exhumation during the transition from oceanic subduction to continental collision. *Earth and Planetary Science Letters*, *267*, 129–145. doi: 10.1016/j.epsl.2007.11.025

Wessel, P., & Smith, W. H. F. (1998). New, improved version of generic mapping tools released. *Eos, Transactions American Geophysical Union*, *79*(47), 579. doi: 10.1029/98EO00426

Wessel, P., & Smith, W. M. F. (2001). New improved version of generic mapping tools released. *EOS Transactions of the American Geophysical Union*, *79*, 579.

Wilks, K. R., & Carter, N. L. (1990). Rheology of some continental lower crustal rocks. *Tectonophysics*, *182*(1-2), 57–77. doi: 10.1016/0040-1951(90)90342-6

Wolf, S. G., & Huismans, R. S. (2019). Mountain building or backarc extension in ocean-continent subduction systems: A function of backarc lithospheric strength and absolute plate velocities. *Journal of Geophysical Research: Solid Earth*, *124*(7), 7461-7482. doi: 10.1029/2018JB017171

Yan, Z., Chen, L., Zuza, A. V., Tang, J., Wan, B., & Meng, Q. (2022). The fate of oceanic plateaus: subduction versus accretion. *Geophysical Journal International*, *231*(2), 1349-1362. doi: 10.1093/gji/ggac266

Yang, S.-H., Li, Z.-H., Gerya, T., Xu, Z.-Q., & Shi, Y.-L. (2018). Dynamics of terrane accretion during seaward continental drifting and oceanic subduction: Numerical modeling and implications for the jurassic crustal growth of the lhasa terrane, tibet. *Tectonophysics*, *746*, 212-228. doi: 10.1016/j.tecto.2017.07.018

Yuan, X. P., Braun, J., Guerit, L., Rouby, D., & Cordonnier, G. (2019). A new efficient method to solve the stream power law model taking into account sediment deposition. *Journal of Geophysical Research: Earth Surface*, *124*(6), 1346-1365. doi: 10.1029/2018JF004867

Yuan, X. P., Braun, J., Guerit, L., Simon, B., Bovy, B., Rouby, D., ... Jiao, R. (2019). Linking continental erosion to marine sediment transport and deposition: A new implicit and o(n) method for inverse analysis. *Earth and Planetary Science Letters*, *524*, 115728. doi: 10.1016/j.epsl.2019.115728